Monthly Notices of the ROYAL ASTRONOMICAL SOCIETY

MNRAS **536,** 203–222 (2025) https://doi.org/10.1093/mnras/stae2606
Advance Access publication 2024 November 21

A coronal mass ejection encountered by four spacecraft within 1 au from the Sun: ensemble modelling of propagation and magnetic structure

Erika Palmerio [1]★ Christina Kay [2] Nada Al-Haddad [3] Benjamin J. Lynch [4,5] Domenico Trotta [6] Wenyuan Yu [3] Vincent E. Ledvina [7] Beatriz Sánchez-Cano [8] Pete Riley [1] Daniel Heyner [9] Daniel Schmid [10] David Fischer [10] Ingo Richter [9] and Hans-Ulrich Auster [9]

[1] *Predictive Science Inc., San Diego, CA 92121, USA*
[2] *The Johns Hopkins University Applied Physics Laboratory, Laurel, MD 20723, USA*
[3] *Space Science Center, University of New Hampshire, Durham, NH 03824, USA*
[4] *Department of Earth, Planetary, and Space Sciences, University of California, Los Angeles, CA 90095, USA*
[5] *Space Sciences Laboratory, University of California, Berkeley, CA 94720, USA*
[6] *The Blackett Laboratory, Department of Physics, Imperial College London, London SW7 2AZ, UK*
[7] *Geophysical Institute, University of Alaska Fairbanks, Fairbanks, AK 99775, USA*
[8] *School of Physics and Astronomy, University of Leicester, Leicester LE1 7RH, UK*
[9] *Institut für Geophysik und extraterrestrische Physik, TU Braunschweig, D-38106 Braunschweig, Germany*
[10] *Space Research Institute, Austrian Academy of Sciences, A-8042 Graz, Austria*

Accepted 2024 November 19. Received 2024 October 28; in original form 2024 August 31

ABSTRACT

Understanding and predicting the structure and evolution of coronal mass ejections (CMEs) in the heliosphere remains one of the most sought-after goals in heliophysics and space weather research. A powerful tool for improving current knowledge and capabilities consists of multispacecraft observations of the same event, which take place when two or more spacecraft fortuitously find themselves in the path of a single CME. Multiprobe events can not only supply useful data to evaluate the large-scale of CMEs from 1D *in situ* trajectories, but also provide additional constraints and validation opportunities for CME propagation models. In this work, we analyse and simulate the coronal and heliospheric evolution of a slow, streamer-blowout CME that erupted on 2021 September 23 and was encountered *in situ* by four spacecraft approximately equally distributed in heliocentric distance between 0.4 and 1 au. We employ the Open Solar Physics Rapid Ensemble Information modelling suite in ensemble mode to predict the CME arrival and structure in a hindcast fashion and to compute the 'best-fitting' solutions at the different spacecraft individually and together. We find that the spread in the predicted quantities increases with heliocentric distance, suggesting that there may be a maximum (angular and radial) separation between an inner and an outer probe beyond which estimates of the *in situ* magnetic field orientation (parametrized by flux rope model geometry) increasingly diverge. We discuss the importance of these exceptional observations and the results of our investigation in the context of advancing our understanding of CME structure and evolution as well as improving space weather forecasts.

Key words: methods: data analysis – methods: numerical – Sun: activity – Sun: coronal mass ejections (CMEs) – Sun: heliosphere – solar wind.

1 INTRODUCTION

One of the ultimate goals in heliophysics is to achieve a full characterization of the structure and evolution of coronal mass ejections (CMEs) from their eruption through their heliospheric propagation. This is important not only from a fundamental physics perspective, but also for space weather science and operations, since CMEs are well-known to generally be the drivers of the most intense geomagnetic storms (e.g. Zhang et al. 2007; Temmer 2021). The overall picture that has emerged after a few decades of research is that, irrespective of their pre-eruptive configuration (see Patsourakos et al. 2020, and references therein), CMEs leave the Sun as flux ropes (e.g. Forbes 2000; Green et al. 2018), which consist of bundles of twisted magnetic fields that warp about a central axis. After a phase of rapid acceleration and expansion in the lower corona (e.g. Patsourakos, Vourlidas & Kliem 2010; Balmaceda et al. 2022) due to their large internal pressure compared to the surrounding environment (e.g. Attrill et al. 2007; Zhuang et al. 2022), CMEs tend to propagate in a self-similar fashion (e.g. Démoulin & Dasso 2009; Subramanian et al. 2014) until ∼10–15 au, when they reach pressure balance with the ambient solar wind (e.g. Richardson et al. 2006; von Steiger & Richardson 2006). However, the specific evolution of a given CME may deviate substantially from this idealized scenario due to a multitude of possible factors (e.g. Manchester et al. 2017; Luhmann et al. 2020).

★ E-mail: epalmerio@predsci.com

In most cases, in fact, CMEs do not propagate through a uniform background, but through a structured medium that consists of different solar wind flows (e.g. Maunder et al. 2022; Palmerio et al. 2022b), slow–fast stream interaction regions (e.g. Wang et al. 2014; Al-Shakarchi & Morgan 2018), the heliospheric current/plasma sheet (e.g. Blanco et al. 2011; Liu et al. 2016), and even other CMEs (e.g. Lugaz et al. 2017; Trotta et al. 2024b). Outcomes of these interaction processes include deflections (e.g. Lugaz et al. 2012; Zuccarello et al. 2012), rotations (e.g. Vourlidas et al. 2011; Liu et al. 2018), deformations (e.g. Liu et al. 2006; Savani et al. 2010), and erosion (e.g. Ruffenach et al. 2015; Pal, Dash & Nandy 2020). As a result, the magnetic configuration of an erupting flux rope at the Sun that is inferred from remote-sensing observations (see Palmerio et al. 2017, and references therein) may differ more or less dramatically from the one that is then measured *in situ* (e.g. Yurchyshyn et al. 2007; Palmerio et al. 2018; Xie, Gopalswamy & Akiyama 2021). More so, the specific trajectory through a given CME that is sampled by a spacecraft may not even be representative of the structure as a whole because of local distortions (e.g. Owens 2020). To complicate things further, analyses of the *in situ* structure of CMEs are often performed with the aid of flux rope fitting/reconstruction models, each based on a certain geometry and physical assumption. However, studies have shown that different flux rope fitting technique can provide very different results for the same CME (e.g. Riley et al. 2004; Al-Haddad et al. 2013), albeit it appears that the level of agreement across models increases for 'simpler' CMEs that display little signatures of expansion and generally more symmetric magnetic field profiles (e.g. Al-Haddad et al. 2018).

The complexity of the myriad processes dictating CME evolution in interplanetary space, together with the known limitations of the available analysis techniques, make it clear that determining the global configuration of a CME from single-spacecraft measurements is a particularly arduous task. For this reason, a number of studies have attempted to obtain a more complete insight into CME structure and evolution using fortuitous relative configurations of two or more probes that have detected the same event *in situ*. A notable example is the work of Burlaga et al. (1981), who reported observations of a single CME in 1978 January by five spacecraft that were distributed over ∼30° in longitude between ∼1 and 2 au from the Sun. In fact, this was the first study to report that all observing probes detected a 'magnetic loop' structure that is now known as a magnetic cloud, i.e. an ejecta that is characterized by enhanced magnetic field strength, smoothly rotating magnetic field vectors, declining speed profiles, as well as depressed temperature and plasma beta – generally interpreted as the *in situ* signatures of a flux rope. The potential of multispacecraft observations has gained significant traction over recent years, so much so that it is possible nowadays to find a few dedicated catalogues in the existing literature (e.g. Davies et al. 2022; Möstl et al. 2022). However, most multiprobe encounters are realized over arbitrary spatial separations of the observers involved, making it difficult to attribute, for example, structural differences to temporal evolution, to local distortions, or to both (e.g. Riley et al. 2003; Dumbović et al. 2019). Additionally, some events are measured over very large (i.e. of at least a few au) radial separations between the observing probes, in which case not even a near-longitudinal alignment would grant that the exact same structure has been detected due to repeated interactions with the structured background (e.g. Burlaga et al. 2001; Palmerio et al. 2021b). Nevertheless, some studies have attempted to isolate these processes by focusing on events characterized by spacecraft close to radial alignment (e.g. Good et al. 2019; Vršnak et al. 2019; Salman, Winslow & Lugaz 2020; Winslow et al. 2021), or with probes spread in longitude at the

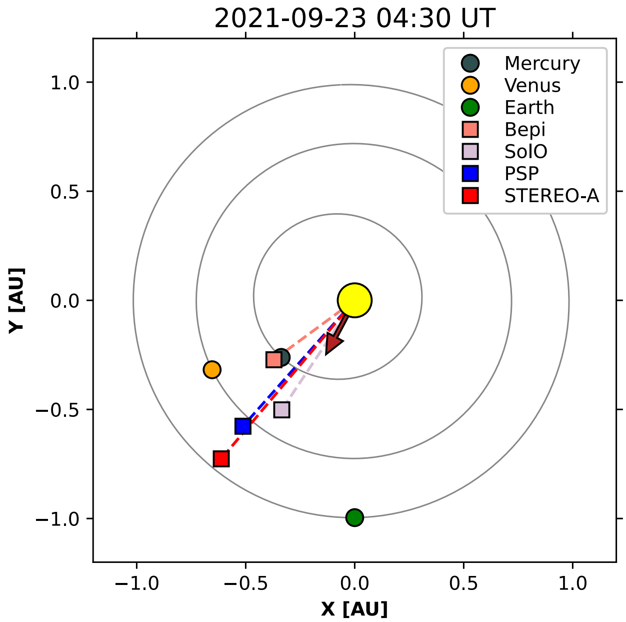

Figure 1. Position of planets and spacecraft within 1 au from the Sun on 2021 September 23 at 04:30 UT, i.e. around the CME eruption time. The longitude of the CME source region is indicated with an arrow emanating from the surface of the Sun. The four probes that encountered the event under study are connected to the centre of the Sun via dashed lines. The orbits of Mercury, Venus, and Earth are also shown.

same radial distance (e.g. Kilpua et al. 2009; Farrugia et al. 2011; Lugaz et al. 2022; Carcaboso et al. 2024), or where observations from two relatively nearby locations are available (e.g. Lugaz et al. 2018; Davies et al. 2021; Palmerio et al. 2024b; Regnault et al. 2024).

As an additional indication that a deep knowledge of CME structure and evolution in the heliosphere is still to be achieved, it is worth remarking that multipoint space weather forecasts of CMEs – or, in the case of heliophysics research, most often hindcasts – have been centred largely on arrival times and/or arrival speeds at multiple locations (e.g. Witasse et al. 2017; Palmerio et al. 2021a) rather than on the magnetic field configurations upon impact (e.g. Asvestari et al. 2021; Sarkar et al. 2024). Truth to be told, this is usually also the case for single-spacecraft encounters (e.g. Riley et al. 2018; Kay et al. 2024) given the well-known challenges associated with magnetic fields forecasts (e.g. Kilpua et al. 2019), but it is only natural to assume that difficulties (and uncertainties) in predicting CME magnetic structure can only increase with the number of observers available for model–data comparisons. On the other hand, the power of multiprobe events is exactly that they allow for models to be validated not at a single location (e.g. Earth), but throughout a specific interval of a CME's journey away from the Sun, permitting thus to increase our understanding of how it evolves and/or of how its local structure compares to the global one.

In this work, we analyse in detail the inner heliospheric evolution of a CME that erupted on 2021 September 23. The remarkable nature of this event resides in the fact that it was detected *in situ* by four spacecraft that were close to radial alignment and more or less uniformly spread between 0.4 and 1 au (see Fig. 1), namely BepiColombo (Bepi; Benkhoff et al. 2021), Solar Orbiter (SolO; Müller et al. 2020), Parker Solar Probe (PSP; Fox et al. 2016), and Solar Terrestrial Relations Observatory Ahead (STEREO-A; Kaiser et al. 2008). Our aim in studying this fortuitous encounter is to closely follow its evolution from the Sun through the inner heliosphere and to perform a multiprobe hindcast of its structure – i.e. testing how well our models can reproduce the propagation of CME flux ropes at different points in space and time. This manuscript is structured as follows. In Section 2, we provide an overview of the remote-sensing observations associated with the 2021 September 23 eruption. In Section 3, we present and analyse the interplanetary measurements of the CME under study at the four different observers. In Section 4, we perform hindcasts of the event using the Open Solar Physics Rapid Ensemble Information (OSPREI; Kay, Mays & Collado-Vega 2022a) analytical modelling suite, with particular emphasis on the CME magnetic structure. In Section 5, we discuss the 2021 September 23 event from both an observational and a modelling perspective. Finally, in Section 6, we summarize our findings and draw our conclusions.

2 OVERVIEW OF THE SOLAR OBSERVATIONS

The eruption and subsequent coronal propagation of the 2021 September 23 CME analysed in this work were observed in extreme ultraviolet (EUV) and white-light (WL) imagery from two viewpoints, i.e. Earth and the STEREO-A spacecraft. For Earth's perspective, we use solar disc imagery from the Atmospheric Imaging Assembly (AIA; Lemen et al. 2012) onboard the Solar Dynamics Observatory (SDO; Pesnell, Thompson & Chamberlin 2012) as well as coronagraph data from the C2 and C3 cameras part of the Large Angle and Spectrometric Coronagraph (LASCO; Brueckner et al. 1995) onboard the Solar and Heliospheric Observatory (SOHO; Domingo, Fleck & Poland 1995). From STEREO-A, we employ images of the solar disc from the Extreme Ultraviolet Imager (EUVI; Wuelser et al. 2004) and coronagraph data from the COR2 camera, both part of the Sun Earth Connection Coronal and Heliospheric Investigation (Howard et al. 2008) suite. Additionally, we take advantage of magnetograph data collected by the Helioseismic and Magnetic Imager (HMI; Scherrer et al. 2012) onboard SDO.

2.1 Source region and eruption

An overview of the available EUV observations for this event is shown in Fig. 2 and a full-disc animated version is provided in Supplementary Video 1. The Sun appears rather active around the time of interest, with several eruptions lifting off the visible disc as well as the limb from both the Earth and STEREO-A perspectives. The eruptive event that is the main focus of this work originates from NOAA active region (AR) 12871 on 2021 September 23 around 04:30 UT, and is accompanied by an M2.8 flare peaking at 04:42 UT. In STEREO-A imagery (Figs 2 a–b), the CME source region is located on the south-western quadrant and the sequence of events features the eruption itself from the western portion of AR 12871 (on-disc arrow in Fig. 2a), the lift-off of a large double-loop structure (off-limb arrows in Fig. 2a), and the subsequent appearance of an additional set of post-eruption arcades (PEAs) in the eastern portion of AR 12871 (arrow in Fig. 2b). These complex observations can be further interpreted using imagery from Earth orbit, where magnetograph measurements complement the EUV data. From the SDO viewpoint (Figs 2 c–d), the CME source region is located on the south-eastern quadrant and on-disc signatures of the eruption include loops opening and propagating northwards of AR 12871 (see Supplementary Video 1, marked with a yellow dashed curve in Fig. 2c) in addition to the PEA systems identified in STEREO-A imagery (arrows in Figs 2 c–d).

The magnetogram contours shown over the EUV data in Fig. 2(c) reveal a complex structure of the local photosphere, with different

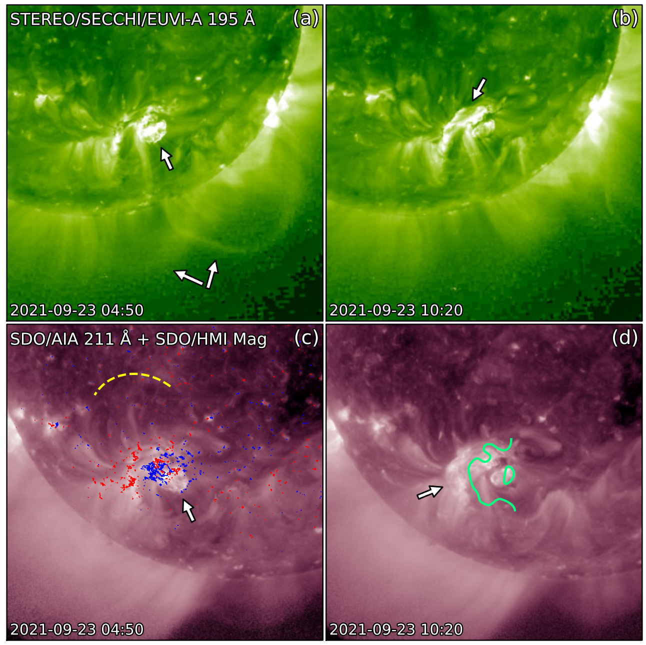

Figure 2. Overview of some EUV observations available for the 2021 September 23 eruption, from the (a–b) STEREO-A and (c–d) SDO (Earth) perspectives. In the bottom panels, EUV observations are complemented by (c) magnetogram contours saturated at ±150 G (red: positive polarity; blue: negative polarity), and (d) the PIL associated with AR 12 871 (solid line contour), obtained from smoothed magnetograph data. Throughout the panels, the various arrows and the dashed arc highlight interesting features associated with the eruption (see the main text for details).

polarity patches forming nested flux systems – distinct regions of closed flux embedded within the larger scale flux system of a coronal streamer (e.g. Longcope 2005; Karpen et al. 2024). Such a configuration tends to result in curved polarity inversion lines (PILs), with a separatrix dome at the interface between different polarities (e.g. Wyper & DeVore 2016; Wyper et al. 2016), as is evident from the PIL contours displayed in Fig. 2(d). This is also a structure that often generates circular-ribbon flares (e.g. Lee et al. 2020; Zhang 2024). The closed-field topology of AR 12871 lies beneath a helmet streamer that is largely east–west oriented, curves around the approximately C-shaped PIL, and continues back towards the west.

In Supplementary Video 1, the first set of PEAs appears at 04:40–04:45 UT with a simultaneous remote brightening at the footpoint of the external spine line (reminiscent of the 'EIT crinkles' of Sterling & Moore 2001), followed by a clear dimming in AIA 211 Å imagery surrounding the dome and a whole loop-shaped region along the external spine flux tube connecting the dome and the remote brightening area. This coincides exactly with the eruption and expansion of the overlapping off-limb loops in the EUVI 195 Å data. The apparent overlap of these loops results from emission of different structures in the optically thin corona being summed during the line-of-sight integration, as these are two different parts of the same streamer belt flux system making the U-turn. The second, more southern (in projection) loop is more diffuse in emission, but expands and erupts essentially in tandem with the more resolved, westward loop. The AIA 211 Å on-disc dimmings follow the EUVI 195 Å off-limb erupting loops, suggesting that the westward loop portion of the helmet streamer is approximately 'above' the circular-ribbon flare while the southern loop portion is approximately 'above' the second set of PEAs along the northern half of the C-shaped PIL. The

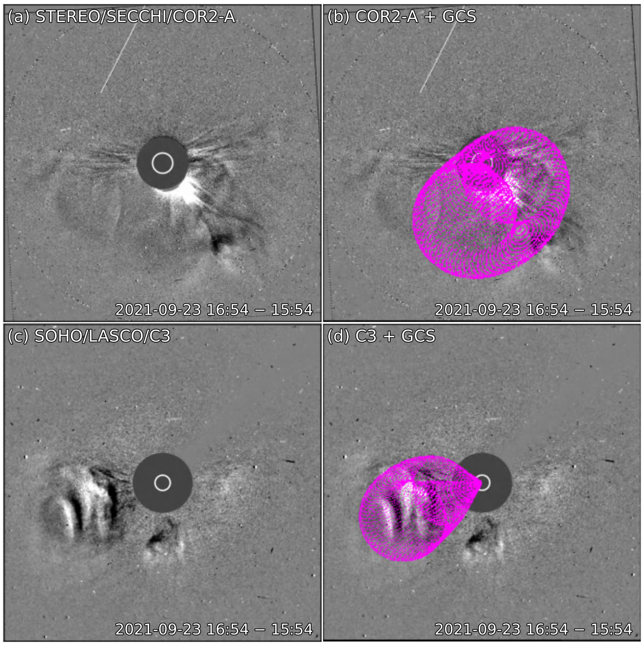

Figure 3. The faint 2021 September 23 CME observed in WL imagery from (top) STEREO-A and (bottom) SOHO. The left panels show plain coronagraph difference images, while the right panels display the same data with the GCS wireframe overlaid.

external spine loop from the initial eruption starts brightening again after ∼07:00 UT (as in Lee et al. 2020), which is followed thereafter by the dimming areas above and below the second PEA gradually returning to their original intensities. Regardless of the specific form of the large-scale helmet streamer energization, a sufficient expansion (gradual or rapid) of the middle-to-outer layers of the streamer belt closed flux system has been shown to erupt as a streamer-blowout CME (Lynch et al. 2016, and references therein).

2.2 Coronal evolution

An overview of the available WL observations for this event is shown in Fig. 3 and an animated version is provided in Supplementary Video 2. In imagery from both viewpoints (i.e. STEREO-A and SOHO), it is clear that multiple faint eruptions are concurrently present at any time over the period of interest, making interpretation of the different structures (and their origin) especially challenging. In particular, the sequence of events evident in coronagraph data include (in relation to the STEREO-A viewpoint): (1) a streamer blowout originating from near the south-eastern limb and emerging around 06:00 UT, (2) a jet-like CME associated with the first set of PEAs described in Section 2.1 and propagating towards the south-west also around 06:00 UT, (3) a large-scale streamer blowout associated with the second set of PEAs described in Section 2.1 and appearing as a (partial) halo starting around 08:00 UT, and (4) an additional jet-like CME related to a later (∼15:30 UT) eruption from AR 12871 visible from around 16:30 UT. Hence, the eruptive event that is the focus of this work is the result of a multistage nested-flux system eruption of the Karpen et al. (2024) type, where the first dome-shaped PEA and remote brightening creates a significant enough disturbance in the streamer flux system that some previously closed flux opens and that erupting plasma makes it into the open field and solar wind. This jet-like transient triggers a more traditional streamer-blowout eruption above the adjacent PIL leading to the partial halo CME (see Pal et al. 2022, for another example of a jet destabilizing an energized, multipolar flux system). Since both jets appear rather narrow as well as southwards-directed and the first streamer blowout propagates mainly off the eastern limb (its corresponding solar eruption can be observed in Supplementary Video 1 off the south-eastern quadrant around 01:00 UT from STEREO-A's perspective), in the following we shall focus on the second streamer blowout, i.e. the eruption associated with the second set of PEAs described in Section 2.1 and that is expected to be encountered *in situ* by the four nearly aligned spacecraft shown in Fig. 1.

To obtain a first-order assessment of the CME morphology and kinematics through the solar corona, we apply the Graduated Cylindrical Shell (GCS; Thernisien 2011) model to nearly simultaneous imagery from STEREO-A and SOHO. The technique consists of manually fitting a parametrized shell (with six free parameters) on to coronagraph imagery, and results at one sample time are shown in the right panels of Fig. 3. According to the performed reconstructions, the CME propagates in the direction $(\theta, \phi) = (-8°, -37°)$ in Stonyhurst coordinates with a moderate inclination (40° counterclockwise from solar west) to the solar equatorial plane and a slow (∼400 km s^{-1}) speed, as is often the case for streamer blowouts (e.g. Vourlidas & Webb 2018). We remark that, apart from uncertainties intrinsic to coronal reconstruction methods performed 'by eye' (e.g. Verbeke et al. 2023; Kay & Palmerio 2024), this specific event is characterized by additional ambiguities due to both its faint nature and its overlapping with other eruptions in projected plane-of-sky images. In fact, it is especially difficult to clearly distinguish the fronts of the two streamer blowouts mentioned above, the second of which is our CME of interest. We do not exclude that the two eruptions may have interacted via their flanks, but since their nose trajectories differ by ∼35° in longitude (determined after performing separate GCS reconstructions of both structures), it is expected that the *in situ* encounters presented in the next section were realized for the most part with the partial-halo CME.

3 ANALYSIS OF THE INTERPLANETARY DATA

Here, we analyse in detail the magnetic field and plasma measurements of the 2021 September 23 CME at the four probes of interest, i.e. Bepi, SolO, PSP, and STEREO-A. An overview of the *in situ* measurements collected by the four spacecraft is shown in Fig. 4, and their evolving heliospheric coordinates at the eruption time and as the CME-driven shock impacted each observer are reported in Table 1. Additionally, to evaluate the overall large-scale evolution of the CME through the inner heliosphere and to confirm that the same eruption likely impacted all the four targets, we have performed a magnetohydrodynamic (MHD) simulation using the coupled Wang–Sheeley–Arge (WSA; Arge et al. 2004) Enlil (Odstrcil 2003) model – these results are summarized in Appendix A.

From each set of spacecraft measurements, we search for various *in situ* CME signatures (e.g. Zurbuchen & Richardson 2006; Kilpua, Koskinen & Pulkkinen 2017) and identify the passage times of the interplanetary shock, sheath region, and CME ejecta. We also determine the boundaries of the 'core' flux rope, i.e. the period in the *in situ* time series characterized by clear magnetic cloud signatures such as smoothly rotating magnetic field vectors and low plasma beta – and that may or may not coincide with the extent of the CME ejecta as a whole (e.g. Richardson & Cane 2010; Kilpua et al. 2013).

We also perform a local shock parameter estimation analysis for all the spacecraft crossings, computing the shock normal ($\hat{n}_{RTN}$), shock

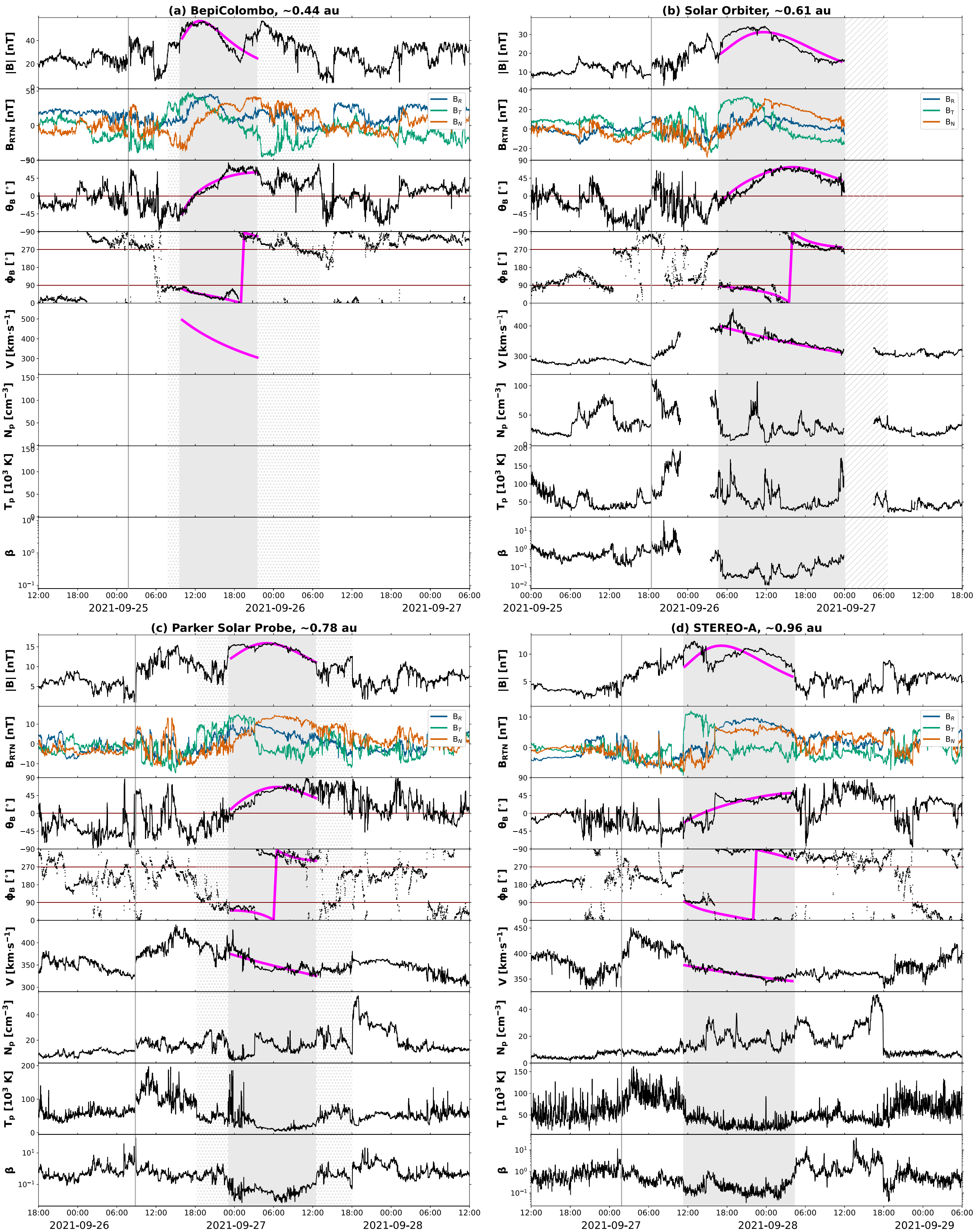

Figure 4. *In situ* measurements of the 2021 September 23 CME at (a) Bepi, (b) SolO, (c) PSP, and (d) STEREO-A. Each plot shows, from top to bottom: magnetic field magnitude, magnetic field components in Radial–Tangential–Normal (RTN) coordinates, latitudinal and longitudinal angles of the magnetic field, solar wind bulk speed, proton density and temperature, and plasma beta. Interplanetary shocks arrivals are marked with vertical areas, while CME ejecta regions are highlighted with shading – the core flux rope in solid colour and other ejecta boundaries in dotted (Bepi and PSP) or hatched (SolO) markings – see the main text for details. The thick curves within the solid shaded regions show flux rope fitting results using the EFF model. The heliocentric distances reported on top of each plot refer to the respective shock arrival time at each spacecraft (see also Table 1). Note that each panel displays 2.75 d of data.

Table 1. Stonyhurst heliographic coordinates in terms of $[r, \theta, \phi]$ triplets (units of [au, deg, deg]) of the four spacecraft at the time of the eruption of the 2021 September 23 CME as well as at the times of the interplanetary shock arrival at each observer.

	Eruption 2021-09-23T04:30	Shock at Bepi 2021-09-25T01:46	Shock at SolO 2021-09-25T18:25	Shock at PSP 2021-09-26T08:50	Shock at ST-A 2021-09-27T01:51
Bepi	[0.46, −0.3, −53.7]	[0.44, −0.1, −49.3]	[0.44, −0.1, −47.6]	[0.43, −0.0, −45.9]	[0.42, +0.1, −44.1]
SolO	[0.60, +1.7, −33.7]	[0.61, +1.8, −31.1]	[0.61, +1.9, −30.1]	[0.61, +1.9, −29.2]	[0.62, +2.0, −28.4]
PSP	[0.77, +3.5, −41.6]	[0.78, +3.5, −42.3]	[0.78, +3.5, −42.6]	[0.78, +3.5, −42.9]	[0.78, +3.5, −43.1]
ST-A	[0.96, +6.7, −40.1]	[0.96, +6.8, −40.0]	[0.96, +6.8, −39.9]	[0.96, +6.8, −39.9]	[0.96, +6.9, −39.8]

Table 2. Shock parameters measured at each spacecraft. The parameters shown are: shock normal vector ($\hat{n}_{RTN}$), shock angle (θ_{Bn}), magnetic compression ratio (r_B), gas compression ratio (r_n), shock speed (V_{sh}), as well as fast magnetosonic and Alfvénic Mach numbers (M_{fms} and M_A, respectively). The shock normals are shown in the RTN frame of reference, with θ_{Bn} expressed in degrees. The shock speed v_{sh} is expressed in km s^{-1} and it is aligned with the shock normal.

	$\hat{n}_{RTN}$	θ_{Bn}	r_B	r_n	V_{sh}	M_{fms}	M_A
Bepi	[0.82, −0.36, −0.44]	18	1.7	–	–	–	–
SolO	[0.88, 0.10, −0.47]	27	1.5	3.3	299	1.7	1.5
PSP	[0.91, 0.34, −0.23]	71	1.8	3.0	347	2.0	1.9
ST-A	[0.50, 0.83, −0.25]	13	2.8	–	–	–	–

Table 3. Flux rope fitting results at each spacecraft. The parameters shown are latitudinal (Θ_0) and longitudinal (Φ_0) directions of the flux rope axis, axial magnetic field magnitude (B_0), chirality (H), normalized impact parameter over the flux rope's radius (p_0), expansion time (τ_{exp}), and normalized goodness-of-fit measure (chi-squared) over the magnetic field components (χ^2_{dir}) as well as magnitude (χ^2_{mag}).

	Θ_0	Φ_0	B_0	H	p_0	τ_{exp}	χ^2_{dir}	χ^2_{mag}
Bepi	39°	46°	82 nT	+ 1	0.23	20 h	0.11	0.94
SolO	68°	49°	38 nT	+ 1	0.06	74 h	0.06	0.43
PSP	69°	167°	23 nT	+ 1	0.68	89 h	0.15	0.06
ST-A	14°	11°	15 nT	+ 1	−0.28	57 h	0.19	0.31

normal angle (θ_{Bn}), magnetic and gas compression ratios (r_B and r_n, respectively), shock speed (V_{sh}), as well as the fast magnetosonic and Alfvénic Mach numbers (M_{fms} and M_A, respectively). The latter two are defined as the ratio between the shock speed and the upstream fast magnetosonic and Alfvén speeds, respectively. When both magnetic field and plasma data are available, we compute the shock normal with the Mixed Mode Method 3 (Abraham-Shrauner & Yun 1976), and the shock speed along the shock normal and in the spacecraft reference frame with the mass–flux conservation. When the magnetic field information is available, the shock normal angle is computed using the magnetic coplanarity theorem (Colburn & Sonett 1966). For a detailed description of these techniques, we refer the reader to Paschmann & Schwartz (2000). For the averaging operation involved in the shock parameters, we use a collection of upstream/downstream windows that we vary systematically from 1 to 8 min using the SERPYSHOCK code (Trotta et al. 2022). Results are summarized in Table 2.

Additionally, at each spacecraft, we perform a fit of the corresponding core flux rope interval using an expansion-modified force-free (EFF; e.g. Farrugia et al. 1993; Yu et al. 2022) model, which takes the classic constant-α force-free solution (e.g. Burlaga 1988; Lepping, Jones & Burlaga 1990) and adds a time-scale parameter that describes the self-similar CME expansion rate (τ_{exp}). The remaining quantities retrieved by the fitting method are axis orientation (Θ_0, Φ_0), field magnitude along the axis (B_0), flux rope chirality (or handedness, H), and impact parameter (p_0, i.e. the crossing distance to the symmetry axis normalized by the cross-sectional radius). Since CME expansion rate can be indirectly estimated from the speed profile (e.g. Owens et al. 2005; Nieves-Chinchilla et al. 2018a), in addition to the magnetic field components we include, where possible, the solar wind speed among the flux rope proprieties constraining the fit. The flux rope fitting results at the four probes are reported in Table 3. In the remainder of this section, we describe in detail observations and analysis of the 2021 September 23 CME *in situ* measurements at each impacted spacecraft.

3.1 Observations at BepiColombo

In situ measurements at Bepi, located at ∼0.44 au during the event, are displayed in Fig. 4(a). Magnetic field data are supplied by the Mercury Planetary Orbiter Magnetometer (Heyner et al. 2021), while no plasma moments are available during the period under investigation – and more generally during most of the cruise phase. The first CME signatures appear at Bepi by means of an interplanetary shock passage on September 25 at 01:46 UT (vertical line in Fig. 4a), characterized by a moderate magnetic field jump and a quasi-parallel nature (see Table 2) – we remark that, due to the lack of plasma data, it is not possible to determine with certainty whether this feature is a full-fledged shock. The following sheath region displays elevated magnetic field magnitudes for approximately two-thirds of its duration and subsequently dips to lower-than-ambient values. The identified CME ejecta period (dotted and solid grey shading in Fig. 4a) features a complex magnetic field profile, characterized by two separate peaks – possibly the signature of an encounter that cuts first through the flank of the frontal CME body and then through the leg (as expected from the WSA–Enlil results shown in Appendix A) or the outcome of interaction of the 2021 September 23 CME with the preceding streamer blowout to its east (described in Section 2.2). In fact, Bepi is the easternmost observer with respect to the CME nose among the four spacecraft at the time of impact, hence both the encounter with a flank and/or leg, as well as the detection of interaction signatures between the two slow streamer-blowout CMEs, can be reasonably expected.

Within the overall CME ejecta interval (bounded by the dotted areas in Fig. 4a) we identify a region of smoother and rotating magnetic field vectors (especially in the north–south component; solid area in Fig. 4a), which we attribute to the core flux rope. Fitting with the EFF model yields a right-handed, moderately inclined rope with a rather low impact parameter (see Table 3). We remark, however, that in this case the speed of the flux rope, being unavailable at Bepi, is not used as a fit-constraining input, but is rather an output of the fitting procedure – given the rather high (∼500 km s^{-1}) resulting leading edge speed compared to the CME speed in the corona (∼390 km s^{-1}), it is likely that a fit employing actual plasma data would have generated somewhat different results.

3.2 Observations at Solar Orbiter

In situ measurements at SolO, located at ∼0.61 au during the event, are displayed in Fig. 4(b). Data are provided by the Magnetometer (Horbury et al. 2020) for magnetic field and the Proton and Alpha particle Sensor of the Solar Wind Analyser (Owen et al. 2020) for plasma parameters. The interplanetary shock driven by the 2021 September 23 CME is observed at SolO on September 25 at 18:25 UT (vertical line in Fig. 4b) and is characterized by a quasi-parallel nature and moderate strength (both Mach numbers are below 2, see Table 2). After the passage of the following sheath region, which displays progressively increasing magnetic field magnitudes, we identify a CME ejecta interval with clear flux rope signatures (solid shading in Fig. 4b). Unfortunately, a concurrent data gap in the magnetic field and plasma measurements prevents us from determining the trailing edge of the structure, but a likely upper limit is indicated by the hatched area in in Fig. 4b) – i.e. we do not expect the CME ejecta to extend past that point, displaying a flat speed profile in contrast to the decreasing trend visible within the flux rope interval.

The magnetic field profile within the ejecta features a ‘classic’ asymmetry in magnitude skewed towards the front of the rope, indicating CME expansion during propagation (e.g. Démoulin & Dasso 2009; Nieves-Chinchilla et al. 2018a). In this case, the flux rope fitting is performed throughout the CME ejecta, from its leading edge up to the data gap, since flux rope signatures are displayed over the whole interval. The EFF model yields a central encounter with a right-handed, highly inclined rope (see Table 3). Despite the fitting results appearing visually ‘good’ (Fig. 4b), we remark that the very trailing portion of the ejecta (of unknown duration) is not included in the calculation, hence the real flux rope axial inclination may have been somewhat different than in our results.

3.3 Observations at Parker Solar Probe

In situ measurements at PSP, located at ∼0.78 au during the event, are displayed in Fig. 4(c). Data are collected by the fluxgate magnetometer part of the FIELDS (Bale et al. 2016) instrument and the Solar Probe Cup (Case et al. 2020) part of the Solar Wind Electrons Alphas and Protons (Kasper et al. 2016) investigation. The sequence of events begins with a clear interplanetary shock passing the spacecraft on 2021 September 26 at 08:50 UT (vertical line in Fig. 4c), characterized by a quasi-perpendicular nature and higher strength than at SolO in terms of speed and Mach numbers (see Table 2). The magnetic field magnitude in the sheath region displays the most symmetric profile amongst the four spacecraft. Ejecta signatures (dotted and solid shaded area in Fig. 4c) follow immediately after; however, besides the central portion that displays clear flux rope characteristics and a symmetric magnetic field magnitude profile (solid shading in Fig. 4c), the outer regions appear to preserve the rotation in the north–south direction but with highly fluctuating fields, possibly due to erosion of the original rope due to reconnection with the ambient solar wind (e.g. Lavraud, Owens & Rouillard 2011; Ruffenach et al. 2012).

Flux rope fitting of the core flux rope interval yields a right-handed, highly inclined rope that is crossed significantly far from its central axis (see Table 3). We also note that the resulting rope axis is oriented rather close to the Sun–spacecraft line, the separation between the two being only 13° in longitude. We remark that possible erosion of the outer layers of the original ejecta, due to interactions with, for example, the ambient solar wind, may have altered the overall flux rope structure and orientation during transit. Finally, we note a region of high-density solar wind (but rather low field magnitudes) right after the passage of the ejecta trailing edge, possibly representing the accumulation of post-CME flows (e.g. Webb & Vourlidas 2016) given that there is no indication of a sector boundary crossing until ∼12 h later (note the longitudinal direction of the magnetic field being preserved before and after the CME passage).

3.4 Observations at STEREO-A

In situ measurements at STEREO-A, located at ∼0.96 au during the event, are displayed in Fig. 4(d). Time series come from the Magnetic Field Experiment (Acuña et al. 2008), part of the In situ Measurements of Particles And CME Transients (Luhmann et al. 2008) suite, as well as the Plasma and Suprathermal Ion Composition (Galvin et al. 2008) investigation. We identify the interplanetary shock passage on 2021 September 27 at 01:51 UT (vertical line in Fig. 4d), and characterize it of quasi-parallel nature and associated with a moderate-to-high magnetic field jump (see Table 2). The sheath region, similarly to SolO measurements, displays an increasing profile in magnetic field magnitude. We find flux rope signatures throughout the CME ejecta interval (shaded area in Fig. 4b), but note that the magnetic field magnitude is characterized by a double-peak profile and that the interface between the two peaks displays sharp discontinuities in all magnetic field components.

Flux rope fitting with the EFF model yields a right-handed, lowly inclined structure with its axis separated only by 11° in longitude from the Sun–spacecraft line and that is encountered at intermediate distances from its central axis (see Table 3). We remark that this fit is associated with the largest error in the magnetic field components, likely due to the discontinuities mentioned above. Again, we note a region of high-density wind immediately following the CME ejecta, which may correspond to the similar structure found in PSP data.

4 CME HINDCASTING WITH OSPREI

Here, we present our efforts to simulate the 2021 September 23 CME in a hindcast fashion with the OSPREI[1] modelling suite, which consists of three coupled modules: the Forecasting a CME's Altered Trajectory (ForeCAT; Kay, Opher & Evans 2015) that models CME deflections and rotations in the corona, the Another Type of Ensemble Arrival Time Results (ANTEATR; Kay et al. 2022b) that propagates the CME through interplanetary space and includes the formation of a CME-driven sheath, and the ForeCAT In situ Data Observer (FIDO; Kay & Gopalswamy 2017) that generates synthetic *in situ* profiles (along a time-dependent spacecraft trajectory or any point of choice). For more information on each module and additional technical details regarding OSPREI, we refer the reader to Kay et al. (2022a). OSPREI is a computationally efficient analytical CME propagation model, which means that, despite the simplified physics compared to, for example, MHD calculations, it can be run with rapid turnaround in ensemble mode (e.g. Kay & Gopalswamy 2018). Hence, in this work, we first design the so-called seed run and evaluate its predicted impacts at the four probes, and then take advantage of a large ensemble (with 200 members) around this baseline run to evaluate the input parameters' influence over the variation in the field and plasma profiles generated at each spacecraft, both individually and together.

[1]https://github.com/ckay314/OSPREI

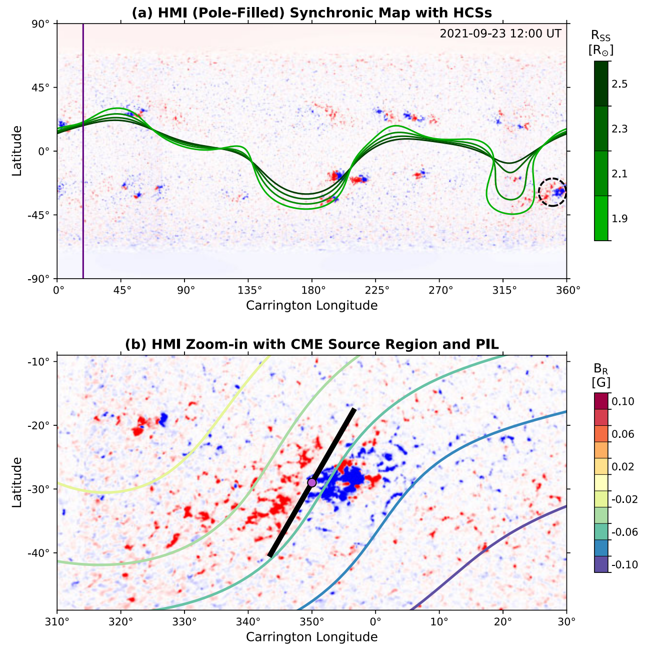

Figure 5. Input photospheric conditions employed for the OSPREI simulation. (a) HMI (pole-filled) synchronic map for 2021-09-23 12:00 UT with the HCS resulting from four different PFSS source surface heights overlaid. The magnetogram has been saturated to ±100 G, with positive (negative) field shown in red (blue). The source region of the 2021 September 23 event is circled, and the Carrington longitude of Earth at the time of the eruption (04:30 UT) is marked with a solid vertical line. (b) Zoom-in on the source region of the 2021 September 23 CME, showing PFSS contours ($R_{SS} = 2.5\,R_\odot$) of the radial magnetic field as well as the location of the flux rope nose (dot at the centre) with its associated PIL (straight thick line).

4.1 Designing the 'seed' run

The first step towards modelling the coronal and heliospheric propagation of CMEs with the OSPREI suite is to define the photospheric boundary conditions. Since the CME of interest erupted $\sim 30^\circ$ away from the Sun–Earth line in longitude, we employ in this study the pole-filled SDO/HMI synchronic map for 2021 September 23, which is generated by replacing from a standard Carrington map daily observations within $\pm 60^\circ$ of the central meridian as seen from Earth (Hayashi et al. 2015). Using this input magnetogram, the coronal conditions – i.e. the coronal magnetic field – are generated by applying the Potential Field Source Surface (PFSS; Wang & Sheeley 1992) model. Since it has been shown that the choice of PFSS source-surface radius (R_{SS}) can have more or less prominent effects on the CME evolution modelled by OSPREI (see Ledvina et al. 2023), we select four source surfaces to test for significant differences in the seed run – the 'classic' $2.5\,R_\odot$ (Altschuler & Newkirk 1969) as well as the lower heights of 2.3, 2.1, and $1.9\,R_\odot$. The input magnetogram, the location of the heliospheric current sheet (HCS) resulting from the different PFSS source surfaces, as well as the source region of the 2021 September 23 CME are shown in Fig. 5(a).

Once the background conditions have been generated, we begin defining the flux rope input parameters, which are listed in detail in Table 4. In the current implementation, OSPREI employs the elliptic-cylindrical (EC; Nieves-Chinchilla et al. 2018b) flux rope model to describe the CME morphology and magnetic configuration. We select the CME initial latitude (θ_0), longitude (ϕ_0), and tilt (ψ_0) based on observations of the active region and its associated PIL (see Fig. 5b). The helicity sign (or chirality, H) is assumed positive based on remote-sensing observations of the eruption (see Palmerio et al. 2017), in particular from the right-skewness of the PEAs with respect to the underlying PIL. Values for CME internal magnetic field (B_{FR}), mass (M_{FR}), and temperature (T_{FR}) are set based on best-guess approximations. Parameters describing CME morphology (AW, $AW_\perp$, δ_{AX}, and δ_{CS}) are loosely based on the GCS reconstructions shown in Fig. 3 and include modifications necessary to grant stability of the EC solution – for example, by elongating the CME half-width along its central axis, yielding a more cylindrical structure against the 'rounded' ellipsoid employed for the WSA–Enlil run (see Appendix A). Properties characterizing CME kinematics in the corona (V_0, a_0, V_1, and a_1) are selected based on off-limb WL observations from SOHO/LASCO. Parameters governing CME propagation in interplanetary space (γ and f_{exp}) are left to their default values. Finally, the background solar wind conditions are defined at the STEREO-A position ($213\,R_\odot$) and scaled with heliocentric distance accordingly to the other locations. The drag coefficient (C_d; e.g. Vršnak et al. 2013) is kept at its default value of one. The values for magnetic field (B_{SW}), density (N_{SW}), and

Table 4. OSPREI input parameters for the seed run and variations employed for the ensemble run. The parameters displayed are, from top to bottom: eruption date and time, radial distance at which coronal propagation (ForeCAT) ends (R_{FC}), flux rope initial height (R_0), latitude (θ_0), Carrington longitude (ϕ_0), and tilt (ψ_0), helicity sign (H), axial magnetic field strength (B_{FR}), CME mass (M_{FR}), CME temperature (T_{FR}), face-on (AW) and edge-on ($AW_\perp$) half-angular width, axial (δ_{AX}) and cross-sectional (δ_{CS}) aspect ratio, initial slow-rise speed (V_0), altitude at which kinematics transition from slow rise to rapid acceleration (a_0), maximum coronal speed (V_1), altitude at which kinematics transition from rapid acceleration to constant speed (a_1), flux rope adiabatic index (γ), interplanetary expansion factor (f_{exp}), heliocentric distance used for the background wind description (R_{SW}), ambient drag coefficient (C_d), as well as solar wind speed (V_{SW}), magnetic field magnitude (B_{SW}), density (N_{SW}), and temperature (T_{SW}).

	Seed	Ensemble
Date	2021-09-23	–
Time	04:30 UT	–
R_{FC}	$20\,R_\odot$	–
R_0	$1.2\,R_\odot$	–
θ_0	-29°	$\pm 3^\circ$
ϕ_0	350°	$\pm 5^\circ$
ψ_0	60°	$\pm 10^\circ$
H	$+1$	–
B_{FR}	2.0×10^3 nT	$\pm 0.5 \times 10^3$ nT
M_{FR}	1.0×10^{16} g	$\pm 0.5 \times 10^{16}$ g
T_{FR}	1.5×10^5 K	$\pm 0.5 \times 10^5$ K
AW	36°	$\pm 5^\circ$
$AW_\perp$	15°	$\pm 2^\circ$
δ_{AX}	0.7	± 0.1
δ_{CS}	0.9	± 0.1
V_0	50 km s^{-1}	± 20 km s^{-1}
a_0	$1.7\,R_\odot$	$\pm 0.1\,R_\odot$
V_1	390 km s^{-1}	± 50 km s^{-1}
a_1	$8.0\,R_\odot$	$\pm 1.0\,R_\odot$
γ	1.33	± 0.1
f_{exp}	0.5	± 0.1
R_{SW}	$213\,R_\odot$	–
C_d	1.0	± 0.25
V_{SW}	340 km s^{-1}	± 40 km s^{-1}
B_{SW}	5 nT	± 3 nT
N_{SW}	10 cm^{-3}	± 5 cm^{-3}
T_{SW}	6.0×10^4 K	$\pm 1.0 \times 10^4$ K

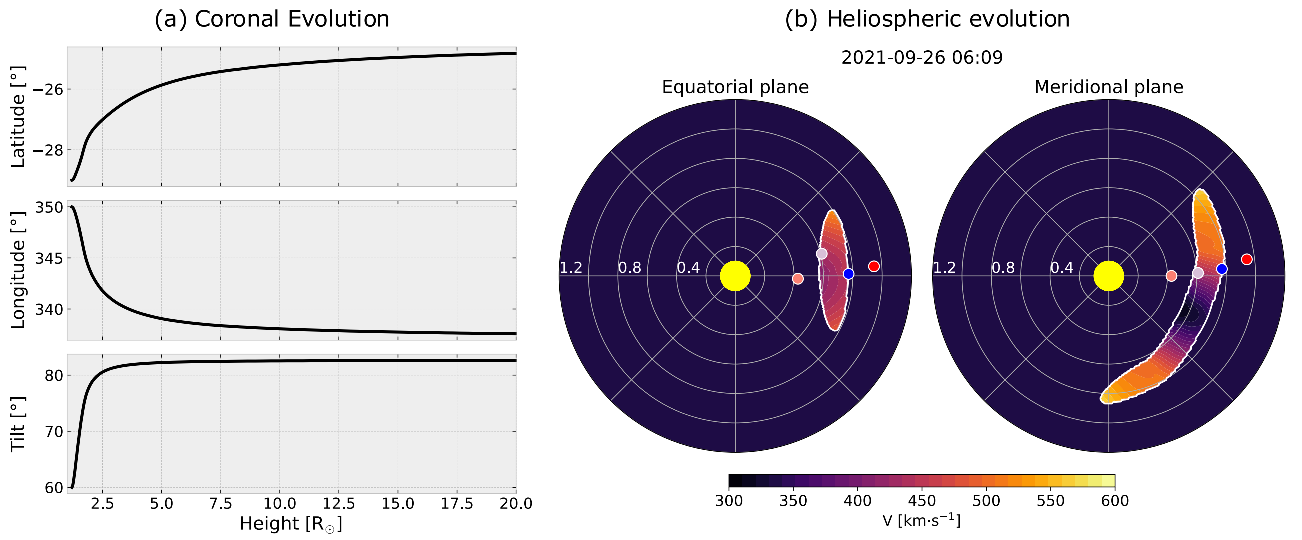

Figure 6. Overview of the (a) coronal and (b) heliospheric evolution of the CME modelled as the seed run for OSPREI. (a) ForeCAT deflections and rotations up to 20 $R_{\odot}$. (b) Snapshot of the CME evolution in interplanetary space as seen from (left) the equatorial and (right) the nose-centred meridional planes. The quantity shown is the solar wind bulk speed, and the four circles represent the positions of the four spacecraft (by increasing distance from the Sun, Bepi, SolO, PSP, and STEREO-A) projected on to the respective planes.

temperature ($T_{\rm SW}$) are taken directly from *in situ* measurements preceding the CME arrival, while the solar wind bulk velocity ($V_{\rm SW}$) is slightly lowered from its STEREO-A values to compensate from the significantly lower speeds found at SolO (note that we are considering a uniform, constant solar wind background speed in this work).

We test the seed run input parameters reported in Table 4 using the four $R_{\rm SS}$ values shown in Fig. 5(a) for the PFSS solution, and find no significant differences in the results. Hence, this particular configuration does not appear to be affected by the PFSS source-surface radius in a notable way, and in the following we shall consider only the 'classic' $R_{\rm SS} = 2.5\,{\rm R}_{\odot}$. And overview of the coronal and heliospheric evolution of the 2021 September 23 CME modelled in the seed run is presented in Fig. 6 and in Supplementary Video 3. In the coronal domain (i.e. the region $\leq 20\,{\rm R}_{\odot}$ where ForeCAT operates), the CME is seen to deflect towards the north-east and to rotate to higher inclinations, its axial parameters changing from $(\theta_0, \phi_0, \psi_0) = (-29^{\circ}, 350^{\circ}, 60^{\circ})$ to $(\theta, \phi, \psi) = (-24.8^{\circ}, 337.6^{\circ}, 82.6^{\circ})$ as shown in Fig. 6(a). In fact, in interplanetary space the CME appears significantly more extended in latitude than in longitude, as can be seen in Fig. 6(b) and Supplementary Video 3. The four spacecraft of interest (Bepi, SolO, PSP, and STEREO-A) are all impacted by the CME north of its nose, with a closer-to-flank encounter at Bepi and a more central one at the remaining three probes.

The OSPREI synthetic *in situ* profiles compared to spacecraft measurements at each location are shown in Fig. 7. The modelled arrival times of shocks/sheaths and ejecta leading edges are all within a few hours of the observed ones, i.e. within the well-known uncertainties (∼10 h) associated with predictions of CME propagation (Kay et al. 2024). The magnetic field magnitude is underestimated at Bepi and SolO, in agreement with *in situ* measurements at PSP, and slightly overestimated at STEREO-A. The individual field components appear to follow the overall west-to-east rotation in B_T and the largely positive nature of B_N, but display opposite sign in B_R compared to observations. In the next section, this seed run is used as the basis for an ensemble run that evaluates the 'best fit' at each spacecraft both separately and when considered together.

4.2 Ensemble modelling

A number of studies have shown that predictions of CME magnetic configuration and/or arrival time can depend more or less strongly on the choice of CME input parameters, even within a single model (e.g. Kay & Nieves-Chinchilla 2021; Palmerio et al. 2022a). To evaluate variations in the synthetic *in situ* profiles due to inputs and to determine differences between individual runs producing the best matches at each spacecraft separately and together, we now consider fluctuations around the seed simulation and run OSPREI in its ensemble mode. We employ a relatively large ($N_{\rm ens} = 200$) number of ensemble members, and the ranges of the variations applied on the input parameters of the seed run are reported in Table 4. The $N_{\rm ens} = 200$ choice is somewhat arbitrary, but reasonably samples the assumed intervals of all the varied parameters. The allowed ranges of variations for each parameter are set to be more conservative (i.e. larger) than what is usually assumed in OSPREI (e.g. Palmerio et al. 2021c; Kay et al. 2022a), to account for the inherent complexity in characterizing both the source region and coronal evolution for the CME under study (see Section 2). In the post-processing phase of the ensemble simulation, we use spacecraft observations at the four locations to compute metrics and thus obtain a 'best fit' for each probe considered both individually and collectively. The goodness-of-fit score is defined as the sum of the fractional mean absolute error of the hourly averages for each magnetic field and plasma parameter together with a timing error consisting of the absolute error in days for all three CME bounds, i.e. shock, ejecta leading edge, and ejecta trailing edge arrivals (see also Kay & Gopalswamy 2017). Within each ensemble member, we also sum the goodness-of-fit scores across each spacecraft to compute a 'global' metric that aims to identify the run that best reproduces the CME behaviour at the four locations when considered together.

An overview of the coronal and heliospheric evolution of the ensemble run is provided in Fig. 8. The coronal evolution of the different ensemble members (Fig. 8a) shows an approximately symmetric (±15°) dispersion in latitude around the seed run, while the ensemble distribution in longitude and tilt have developed a

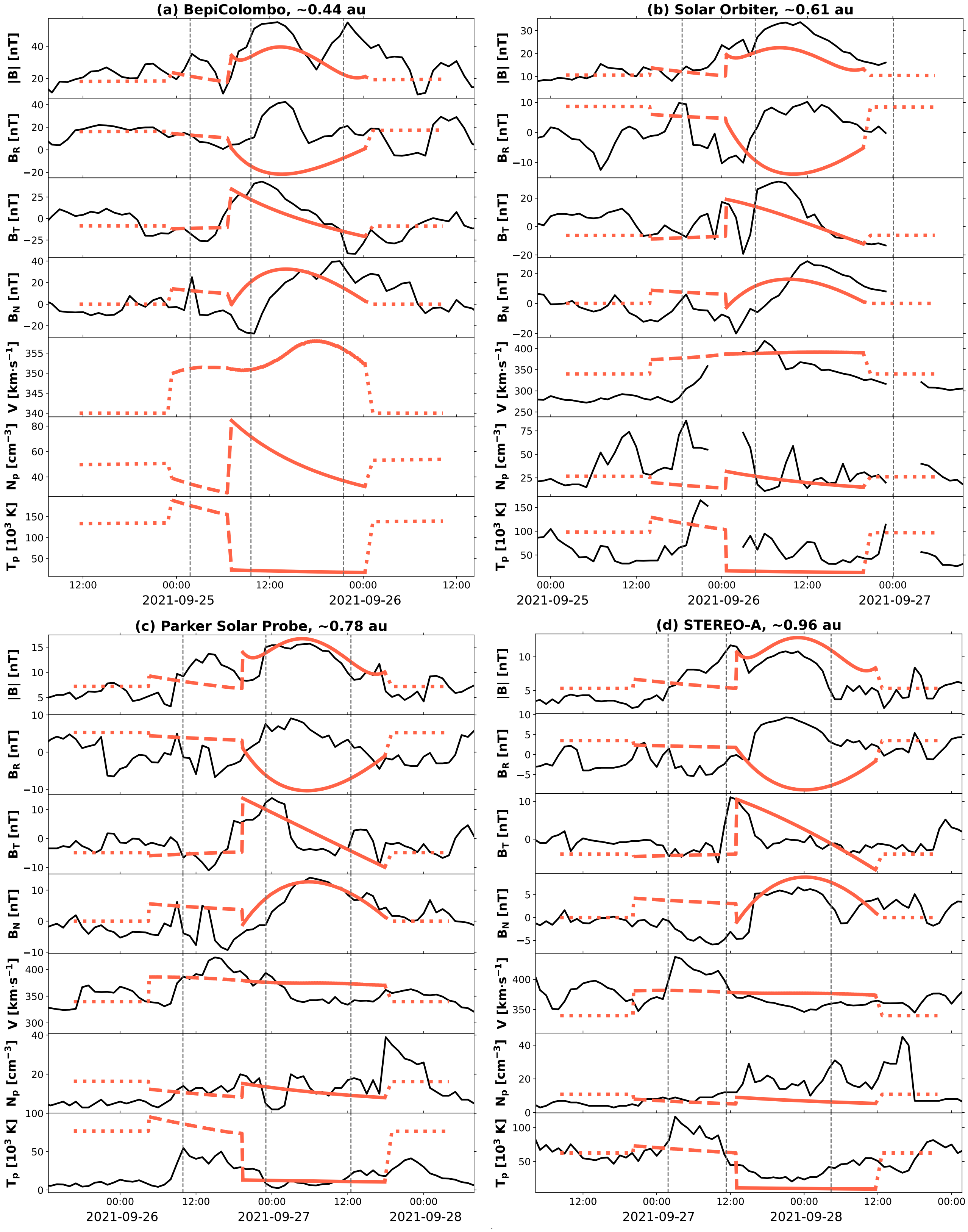

Figure 7. Overview of the OSPREI seed simulation run results shown against *in situ* measurements of the 2021 September 23 CME at (a) Bepi, (b) SolO, (c) PSP, and (d) STEREO-A. Each plot shows, from top to bottom: magnetic field magnitude, magnetic field Cartesian components in RTN coordinates, solar wind bulk speed, as well as proton density and temperature. The spacecraft data are displayed in thinner curves, while the OSPREI synthetic profiles are shown in thicker lines for (dotted) background wind, (dashed) sheath region, and (solid) CME ejecta intervals. The dashed vertical lines mark (leftmost) the shock arrival and (remaining two) the flux rope boundaries as observed by each spacecraft.

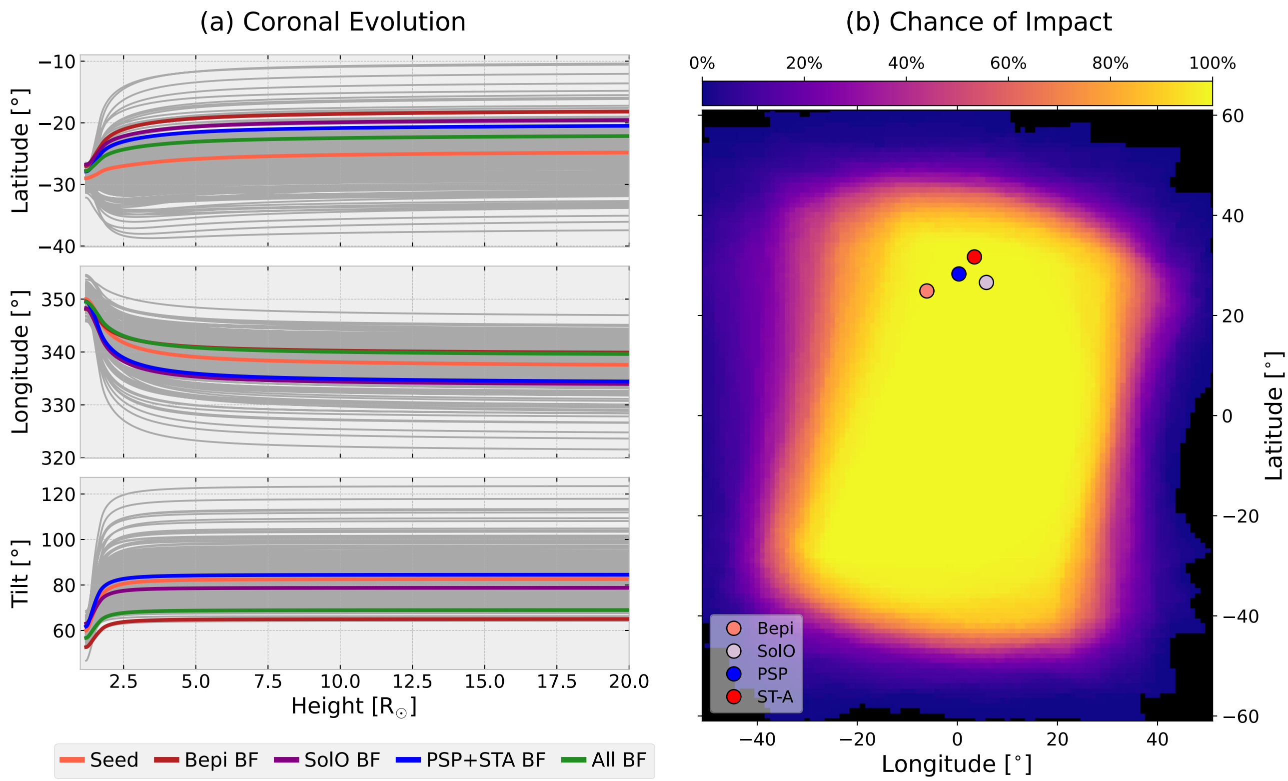

Figure 8. Overview of the (a) coronal and (b) heliospheric evolution of the (200-member) ensemble CME run modelled with OSPREI. (a) ForeCAT deflections and rotations up to 20 $R_\odot$. The seed run as well as the various best-fitting runs are highlighted in thicker, coloured lines with respect to the remaining ensemble members. (b) Radial slice of the CME angular extent at the time of impact at PSP, shown as a heat map representing the chance of impact at a given latitude–longitude coordinate across the ensemble. The superposed circles mark the projected positions of the four spacecraft at their respective observed CME arrival times (i.e. the times shown in Table 1). The figure is displayed in the frame centred at the CME nose of the seed run.

distinct asymmetry by 20 $R_\odot$. The longitude has an extended tail below the seed value and is condensed above it ([−20°, +10°]), whereas the tilt angle shows the opposite trend ([−20°, +40°]). The symmetry found in the latitudinal evolution suggests that the seed is in a relatively balanced location with respect to the magnetic forces. We would expect the global forces to push the CME north towards the HCS, and the local forces to depend on the exact location within the AR. Small changes in the initial position can affect the balance between these forces either way. The persistent eastward motion is likely in large part due to the strong negative polarity region of the AR, but we would also expect some eastward motion from the global forces since that is the direction of the closest part of the HCS. In terms of evolution of the best-fitting runs with respect to the seed, we note that all of them are characterized by higher latitudes throughout the ForeCAT domain, while mixed patterns are visible in the remaining two parameters. In the longitude, the global best-fitting run is slightly westwards of the seed, but the single-spacecraft best-fitting runs are all clustered a few degrees eastwards of the seed – note that a single run gives the best fit at both PSP and STEREO-A, hence they are considered together throughout this analysis. In the axial tilt, the single-spacecraft best-fitting ensemble members for SolO and PSP + STEREO-A are clustered close to the seed, while the Bepi and global best-fitting run are less tilted than the seed by ∼15°. The distribution in coronal evolution evident from Fig. 8(a) results in the CME affecting slightly different angular wedges during its heliospheric propagation across the ensemble, as shown in the heat map of Fig. 8(b). Note that, in OSPREI, the CME size increases with distance as a result of magnetic and thermal forces between the ejecta and the solar wind background, hence the radial slice shown in the figure is arbitrarily chosen at the corresponding impact time at PSP for each ensemble member. The projected positions (at each corresponding arrival time) of the four spacecraft over the CME angular extent show that all probes are located in a region of high chance of impact (>90 per cent) and that all encounters take place north of the CME nose, while the wider distribution in longitude indicates that it depends on the specific run whether a probe crosses the CME east or west of its highly inclined symmetry axis.

The synthetic *in situ* profiles resulting from the ensemble run are shown in Fig. 9, in the same colour-coding as Fig. 8. First of all, we note that most shock/CME arrivals take place within a few hours of the seed but a few runs display larger differences (>12 h), indicating that different combinations of CME initial speed, CME acceleration profile, and/or drag coefficient may result in significantly different predictions even in the case of a fixed, uniform solar wind background. In terms of magnetic configuration, despite more or less prominent differences in the field magnitude all runs tend to follow the seed's overall trend of negative B_R, positive-to-negative rotating B_T, and mostly positive B_N. This is not surprising, since the CME tilt over the ensemble is spread over approximately ±30° around the north direction (90°) and all encounters take place north of the CME nose. With respect to the seed, the single-spacecraft best-fitting runs tend to show a better alignment of the ejecta leading edge with observations with the exception of PSP, where the additional rotation in B_T and B_N preceding what we defined as the flux rope interval

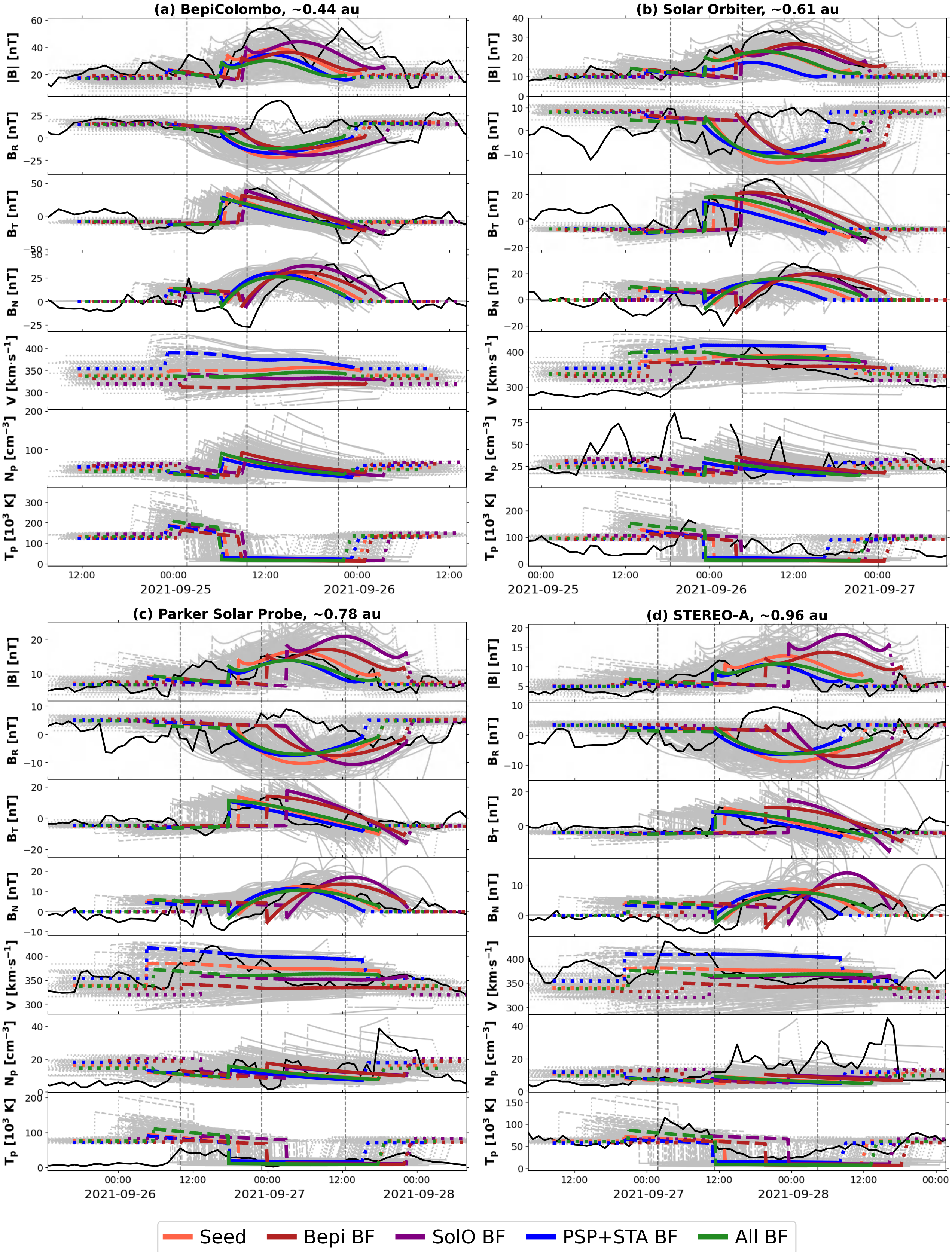

Figure 9. Overview of the OSPREI (200-member) ensemble simulation run results shown against *in situ* measurements of the 2021 September 23 CME at (a) Bepi, (b) SolO, (c) PSP, and (d) STEREO-A. The seed run as well as the various best-fitting runs are highlighted in thicker, coloured lines over the remaining ensemble members. All panels and parameters are shown in the same format as Fig. 7.

(see Section 3.3 and Fig. 4c) appears to be affecting fitting results. The global best-fitting profiles are remarkably similar to the single-spacecraft ones at PSP and STEREO-A, while larger differences are present at Bepi and SolO – this may be due to the two outer probes being characterized by the same single-spacecraft best fit, thus carrying a larger weight in the global best-fitting calculation, but also being located between the two inner probes in longitude, thus 'averaging out' differences due to angular separation. Overall, the seed and best-fitting runs do not show particularly stark differences at any of the locations considered, and all appear approximately in the middle of the ensemble distribution for each curve.

However, despite each best-fitting run being comfortably within the ensemble distribution at each of the four spacecraft individually, the best-fitting ensemble member for a particular inner spacecraft (Bepi and SolO) has no guarantee of it being the best or even a reasonable fit at any of the further spacecraft (PSP and STEREO-A). This is clearly illustrated by the maroon and purple curves shown in Figs 9(c–d), which are the best-fitting ensemble members for Bepi and SolO propagated to the PSP and STEREO-A positions, respectively. The set of best-fitting profiles at Bepi and SolO show relatively minor timing, shape, and magnitude differences between them whereas by the radial distances of PSP and STEREO-A, both the Bepi and SolO ensemble members produce magnetic field profiles that are more prominent outliers in their respective distributions and represent the observational *in situ* data less adequately.

5 DISCUSSION

Observations of the 2021 September 23 CME (Sections 2 and 3) as well as our modelling efforts with OSPREI (Section 4) have shown that the event considered in this work presents many complex characteristics that make both interpretation of the spacecraft measurements and prediction of its heliospheric impact(s) particularly challenging. Here, we synthesize the results and findings presented in the previous sections to build a comprehensive overview of the CME's Sun-to-1 au transit and large-scale structure while still highlighting the complexities and disagreements where they arise.

5.1 The observational perspective

The 2021 September 23 eruption is characterized by a complex, nested-AR source region (Karpen et al. 2024), multistage eruption dynamics, and ambiguous WL signatures. The first (precursor) stage involves a circular ribbon flare in the closed flux region near the edge of the helmet streamer belt (Wyper et al. 2016). The second (main) stage of the eruption generates the CME with a classic two-ribbon flare, which is also associated with simultaneous twin coronal dimmings (Thompson et al. 1998). The CME-producing PEA and its underlying PIL's north–south orientation gives an estimated CME flux rope orientation of west–north–east (WNE; following Bothmer & Schwenn 1998; Mulligan, Russell & Luhmann 1998) for a right-handed flux rope (see also Fig. 5b), which is consistent with the large-scale orientation of the overlying helmet streamer belt. It is not possible to observe in detail the CME deflecting and/or rotating in the corona (e.g. Vourlidas et al. 2011) due to its faint appearance and because of the presence of simultaneous eruptions in the available WL data. Nevertheless, one significant point of interest of this event is that it was encountered *in situ* by four probes approximately equally distributed in heliocentric distance between 0.4 and 1 au; hence, we shall leverage these measurements to compare the estimated CME structure at the Sun with that observed *in situ*, and at the same time to evaluate similarities and differences among the four *in situ* data sets.

At each spacecraft, the first CME-related structure to be measured is the CME-driven shock. Despite the evident difficulties in addressing the shock properties due to the fact that no plasma data (more precisely, speed components) are available at Bepi and STEREO-A, we recover a compatible set of parameters at the different observers, with no strong variations in the compression ratios, shock speeds, and Mach numbers (see Table 2). The shock appears subcritical at both SolO and PSP, a property frequently observed in the case of interplanetary shocks (e.g. Kilpua et al. 2015). We note a level of variability in the local shock normals as shown in Table 2, indicating that local shock properties may vary more or less strongly at different heliospheric locations for a single event. In this regard, the exploitation of multiple heliospheric observers is an invaluable resource to quantify local variability against large-scale evolution effects (see also Palmerio et al. 2024b; Trotta et al. 2024a, for recent efforts in defining CME-driven shock properties in multispacecraft data).

The sheath region immediately following the shock displays different characteristics at the different probes, first and foremost in the profiles of the magnetic field magnitude – increasing towards the ejecta at SolO and STEREO-A, abruptly declining at Bepi, and more plateau-like at PSP (see Fig. 4). At least at the three spacecraft for which plasma data are available, the CME is embedded in the slow solar wind, hence these difference do not appear to be related to the eruption propagating through profoundly different local environments. Nevertheless, previous studies have shown that the structure of CME-driven sheaths may differ more or less significantly both at the local and global level even for multispacecraft encounters realized in radial alignment or in close proximity of the probes involved (see e.g. Good et al. 2020; Kilpua et al. 2021). The measurements investigated here highlight further the importance of reaching a deeper understanding of the complex dynamics between the shock driver and the ambient medium responsible for sheath formation and evolution, especially given their potential to drive severe space weather effects (e.g. Pulkkinen et al. 2007).

Finally, all four probes are impacted by the CME ejecta, where we identify several similarities as well as differences across the different data sets. To aid in this analysis and discussion of its results, Fig. 10 displays the four sets of ejecta magnetic field time series normalized in time, scaled in magnitude, and superposed on to the STEREO-A data (i.e. at the outermost spacecraft). It is clear that the B_T and B_N components follow a very similar trend across the four time series, while larger variability is present in B_R and $|B|$. Visually, the positive-to-negative rotation in B_T and the mostly northwards B_N (with some southwards fields at the ejecta front measured by Bepi and STEREO-A) suggest an overall flux rope type close to the WNE configuration estimated from remote-sensing observations. This is consistent with previous studies, which have shown that the majority of CMEs tend to maintain their axial orientation in interplanetary space within $\pm 45^\circ$ of their solar counterpart (e.g. Palmerio et al. 2018; Xie et al. 2021). Nevertheless, this agreement at the global level is contrasted by some prominent local differences, the most striking of which being the profile of the magnetic field magnitude within the flux rope ejecta. The characteristic shape of the $|B|$ curves – having a distinct, often asymmetric peak offset towards the leading edge of the ejecta – suggests more central encounters at SolO and PSP and more complicated spacecraft crossings at Bepi and STEREO-A (cf. the more variable $|B|$ profiles), or alternatively a rope that is locally distorted. Given the overall agreement in the large-scale trend of the B_T and B_N components at all four spacecraft, the

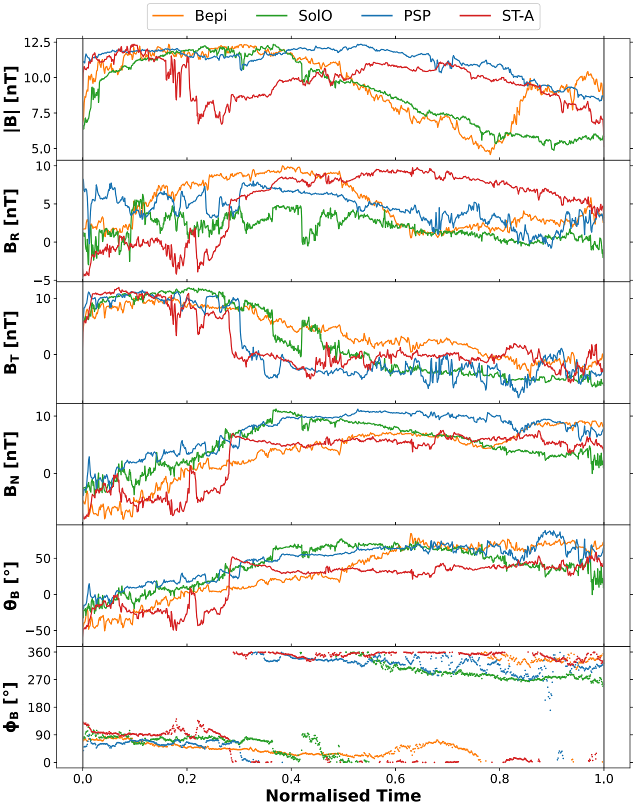

Figure 10. Ejecta magnetic fields of the 2021 September 23 CME as observed by Bepi, SolO, PSP, and STEREO-A, normalized in duration so that each of the leading and trailing edges are aligned. The time series for (from top to bottom) field strength, (RTN) Cartesian field components, and magnetic field angles in the latitudinal (θ_B) and longitudinal (ϕ_B) directions have been scaled in magnitude as to superpose each spacecraft's measurements on to the STEREO-A ones. The scaling factor is obtained by normalizing the maximum magnetic field magnitude at a given probe to the corresponding value at STEREO-A (note that this scaling does not apply to the field angles). For each spacecraft data set, the interval shown corresponds to the flux rope interval (where flux rope fitting is performed, see Fig. 4).

observed variability in $|B|$ appears to be largely due to the differences in each probe's B_R profiles, for example, large-scale B_R polarity changes, HCS proximity, etc. This suggests that the B_R component may contain important information about the relative position of the spacecraft with respect to the CME as well as the CME's orientation with respect to the interplanetary sector structure. Additionally, the flux rope fitting results (Table 3), despite all giving a westerly axial direction ($+\hat{T}$ component), suggest a high-inclination rope (of WNE type) at SolO and PSP, but a low-inclination one (of south–west–north or SWN type) at Bepi and STEREO-A. These fitting results reflect the difference(s) in each event's B_T and B_N profiles. For example, the low-inclination encounters (Bepi and STEREO-A) have larger southern fields (more negative B_N) at the beginning of their CME intervals as well as shallower negative B_T regions in the trailing half of the ejecta compared to the higher inclination encounters at SolO and PSP.

5.2 The modelling perspective

Analytical modelling of the 2021 September 23 CME provides the rare opportunity to validate and compare results at four well-separated locations in the sub-au heliosphere: Bepi (0.44 au), SolO (0.61 au), PSP (0.78 au), and STEREO-A (0.96 au). Forward-modelling of CME propagation and magnetic structure with analytical codes has thus far focused largely on two-spacecraft encounters realized in near-radial alignment (e.g. Möstl et al. 2018; Sarkar et al. 2024), with results suggesting that data collected by an inner probe should be used to constrain models for more accurate predictions at 1 au (e.g. Kubicka et al. 2016; Laker et al. 2024). In this work, we employed the OSPREI modelling suite to evaluate the coronal and heliospheric evolution of the 2021 September 23 CME and to evaluate its impact across interplanetary space via an ensemble approach. After determining that the seed run largely captures the overall structure of the CME at the different probes (see Fig. 7), we computed goodness-of-fit metrics for each ensemble member to extrapolate single-spacecraft and global 'best runs'.

One interesting finding of this analysis is that the various best-fitting solutions show little spread at Bepi, and then progressively diverge with heliocentric distance up to STEREO-A, where the most prominent differences are displayed (see Fig. 9). This is intuitively reasonable, since the effects of CME evolution on *in situ* profiles are expected to become more evident with distance from the Sun. Nevertheless, we remark that the CME modelled here with OSPREI propagates through a constant, uniform solar wind background, hence no additional rotations or deflections take place beyond the coronal domain of the simulation – although the CME can still decelerate, expand, and deform due to its interaction with the ambient medium. Hence, the results presented here show the importance of accurately determining CME input parameters from observations, since small spreads in predictions closer to the Sun can result in broad uncertainties at 1 au even when neglecting additional evolutionary effects in the heliosphere. For example, this is evident when considering the best fit at SolO propagated to STEREO-A, resulting in a CME ejecta arrival ~12 h later than the best STEREO-A run and in magnetic field magnitudes approximately twice as high. When considering predictions at PSP and STEREO-A, on the other hand, we found that the same ensemble run produces the best fit at both spacecraft. The results shown here indicate that there may be a threshold (in terms of radial and angular distance) to the usefulness of inner-probe observations for 1 au predictions, beyond which correlations largely cease – in this work, at their respective CME arrival times STEREO-A is separated by 0.52 au and 12° from Bepi, 0.35 au and 11° from SolO, and 0.18 au and 5° from PSP. Indeed, it has been shown that even in *in situ* CME reconstructions (rather than forward-modelling) reconciling measurements taken at far-separated spacecraft is often not possible under the assumption of self-similar expansion (e.g. Weiss et al. 2021; Davies et al. 2024).

Nevertheless, we remark that in this work we have employed a simple goodness-of-fit metric based on absolute errors between modelled and observed quantities combined with timing errors. In the future, we will consider more sophisticated metrics such as dynamic time warping, which has been shown in recent works to be applicable to solar wind (e.g. Samara et al. 2022; Kieokaew et al. 2024), solar energetic particle (e.g. Palmerio et al. 2024a), and even geomagnetic index (e.g. Laperre, Amaya & Lapenta 2020; Maharana et al. 2024) time series. It is possible that different metrics highlight different solutions as the 'best run', and more work is necessary in this direction to evaluate how to best benchmark CME arrival time and magnetic field configuration within a single, combined metric (see Verbeke et al. 2019, for an overview of some initial efforts on the matter).

Finally, we noted that, even if the observed B_T and B_N components were somewhat well captured by the seed and ensemble member runs (Figs 7 and 9), the B_R component was predicted to have the opposite

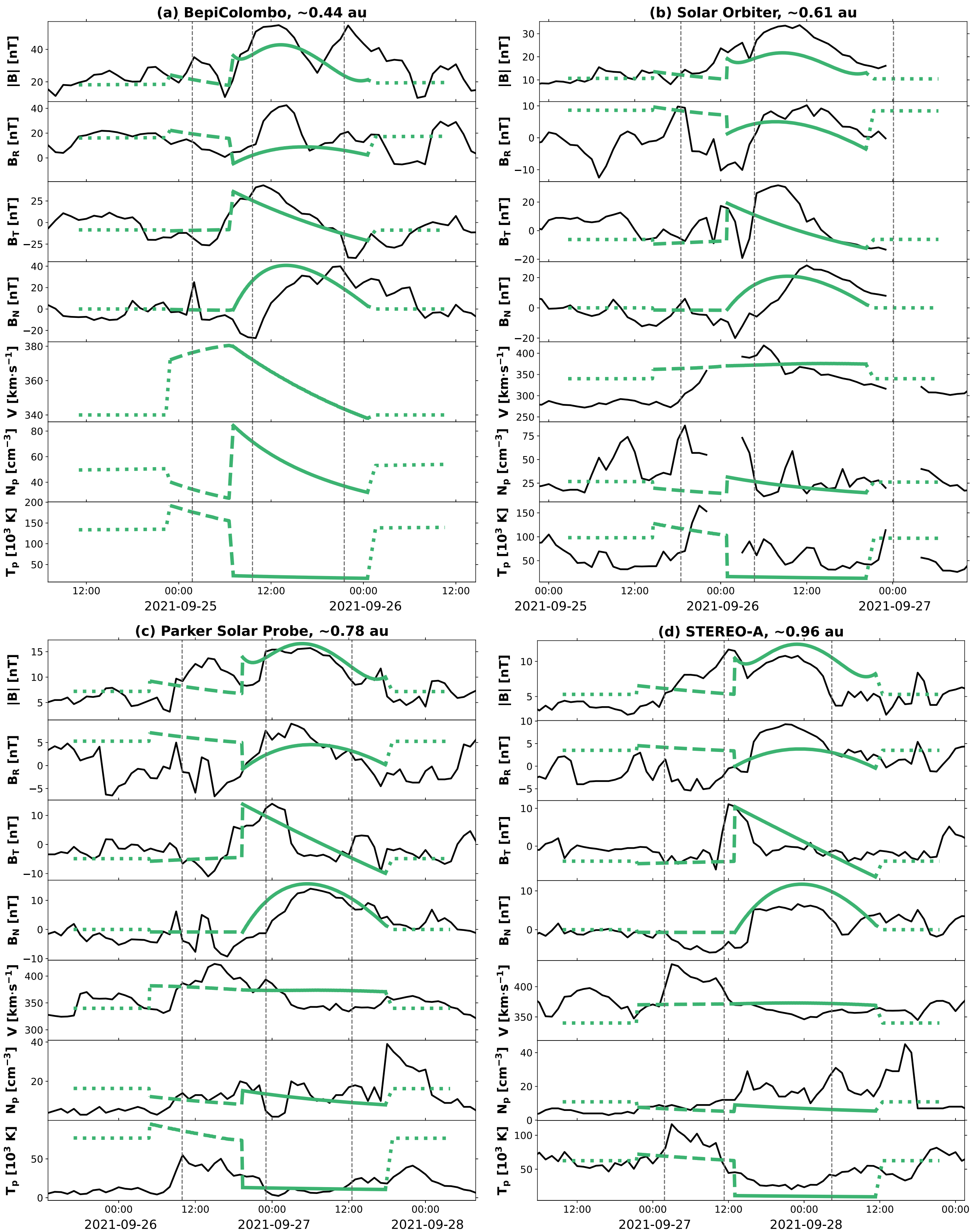

Figure 11. Overview of the OSPREI seed simulation run results with latitudinally mirrored (with respect to the CME nose) spacecraft crossings shown against *in situ* measurements of the 2021 September 23 CME at (a) Bepi, (b) SolO, (c) PSP, and (d) STEREO-A. All panels and parameters are shown in the same format as Fig. 7.

sign for all cases. To verify whether this is indeed a result of all the simulated crossings taking place north of the CME nose (see Fig. 8b), we extract synthetic *in situ* profiles from the seed run by mirroring each spacecraft's position in latitude with respect to the apex (i.e. by considering the corresponding 'minus' Y-coordinates in Fig. 8b), as shown in Fig. 11. Indeed, all B_R predictions inside the ejecta are significantly improved, indicating that the CME may have been crossed, in reality, south of its nose by all four probes. It is possible that the ForeCAT deflections in the corona were underestimated by OSPREI (cf. the nose latitude of only -8° estimated via the GCS reconstructions in Section 2.2 against the seed latitude of -25° in Section 4.1), and/or that the CME further deflected northwards during its interplanetary propagation (e.g. Isavnin, Vourlidas & Kilpua 2014), where we have instead assumed constant trajectory. It is worth noting that OSPREI could also be run in 'interplanetary mode' only, where CME parameters in the outer corona (estimated, e.g. from GCS reconstructions) are propagated directly with ANTEATR + FIDO – thus, bypassing the ForeCAT portion of the modelling suite. In the case of the event studied here, such a run (not shown) yields B_R components that are still negative but significantly closer to zero than in Fig. 7, further suggesting that the CME might have continued its northwards deflection after leaving the solar corona.

6 SUMMARY AND CONCLUSIONS

In this work, we have taken advantage of an exceptional clustering of spacecraft between ∼0.4 and ∼1 au to perform analysis and modelling of the 2021 September 23 CME from its eruption up to its arrival at ∼1 au. To our knowledge, this is the first report of an event being observed *in situ* by four well-radially-separated probes inside 1 au, providing a critical opportunity to evaluate CME evolution across the different locations and to provide additional validation for multispacecraft CME propagation modelling. Overall, the picture that emerges from the synthesis of remote-sensing and *in situ* observations of the 2021 September 23 CME is that of a slow, moderate-sized event that propagated through a slow ambient wind and that largely maintained its magnetic orientation as estimated from solar data. Nevertheless, the *in situ* profiles at the four probes, while following similar trends, are characterized by several prominent differences – especially in the magnetic field magnitude and in a number of discontinuities present only at a subset of spacecraft (see Fig. 10). Given that strong interactions with a structured solar wind are not expected to have taken place in this particular event (since, as mentioned in Section 5.1, the CME is embedded in the slow solar wind at all locations for which plasma data are available), it is possible that distortions over the full CME body are a remnant of the intrinsic complexity of the CME eruption dynamics (see Section 2.1) and coronal evolution (see Section 2.2), which involve a multipolar source region and multiple eruptions close in time. For example, Bothmer & Mrotzek (2017) suggested that kinks in the near-Sun flux rope configuration can propagate through its interplanetary evolution, resulting in a CME body characterized by local deviations from the global structure that may even appear to feature different orientations from one *in situ* encounter to the next.

Modelling of the 2021 September 23 CME with OSPREI showed that the seed run does an adequate job at predicting the various arrival times (which are also consistent with WSA–Enlil + Cone results, see Appendix A) as well as the multispacecraft *in situ* profiles at the large scale in a hindcast fashion (see Fig. 7), but is naturally not capable to reproduce the smaller scale variability encountered in the *in situ* measurements. In this sense, Sun-to-1 au MHD modelling (e.g. Jin et al. 2017; Török et al. 2018) is expected to be better-suited to capture the complex evolution of CME magnetic fields during interplanetary propagation. We noted that the seed run predicted an opposite sign of B_R with respect to spacecraft observations and showed that 'mirroring' the encounters south of the CME nose yields a better match (see Fig. 11), suggesting that the CME deflected further northwards than estimated in our simulations. This exercise highlights the importance of leveraging modelling results to further interpret observational data, where discrepancies in the compared time series can be used to extrapolate and draw conclusions as to the evolution dynamics of a CME. Ensemble modelling with OSPREI revealed that the 'best-fitting' runs across the different spacecraft tend to diverge with heliocentric distance and/or angular separation, indicating that using measurements at an inner probe to constrain predictions at an outer probe is a reasonable approach as long as the two locations are not 'too far apart'. In practical terms, given that PSP (0.78 au) and STEREO-A (0.96 au) were characterized by the same ensemble member resulting in the best-fitting run, it appears reasonable to assume that sub-au probes around Venus's orbit might be an optimal choice to constrain 1 au predictions while allowing for enough leading time (e.g. Szabo et al. 2023).

Finally, analysis and modelling of the 2021 September 23 CME has been possible due to a fortuitous relative configuration of four probes inside 1 au: Bepi, SolO, PSP, and STEREO-A. Multispacecraft CME encounters that involve more than two probes are understandably rare and are often rather complex to interpret, since it becomes increasingly difficult to attribute differences in the measurements to heliospheric evolution (in time) and/or to local distortions (across the CME body). A dedicated constellation with well-defined spatial and angular separations is expected to provide improvements towards resolving such ambiguities (see Scolini et al. 2023, for a detailed numerical study on the amount of probes necessary to fully characterize CME complexity). Nevertheless, as discussed in Palmerio et al. (2023a), this study represents yet another proof of the importance of multispacecraft measurements and of taking advantage of as many data sets as possible, including those from planetary missions (as was the case for Bepi in this work), to bring further insights into the varied aspects of CME evolution in the heliosphere.

ACKNOWLEDGEMENTS

EP, CK, NAH, and WY are supported by NASA's Parker Solar Probe Guest Investigator (PSP-GI; grant no. 80NSSC22K0349) programme. EP and PR acknowledge NSF's Prediction of and Resilience against Extreme Events (PREEVENTS; grant no. ICER-1854790) as well as NASA's Living With a Star (LWS; grant no. 80NSSC24K1108) programmes. BJL acknowledges support from NASA80NSSC21K0731, 80NSSC21K1325, and 80NSSC22K0674, as well as NSF AGS 2147399. VEL is supported by the National Science Foundation Graduate Research Fellowship under grant no. 2235201. BSC acknowledges support from the UK-STFC Ernest Rutherford fellowship ST/V004115/1 and the BepiColombo guest investigator grant ST/Y000439/1.

This study has received funding from the European Union's Horizon 2020 research and innovation programme under grant agreement no. 101004159 (SERPENTINE; www.serpentine-h2020.eu). Views and opinions expressed are, however, those of the authors only and do not necessarily reflect those of the European Union or the European Research Council Executive Agency. Neither the European Union nor the granting authority can be held responsible for them. The authors thank NASA's Community Coordinated Modeling Center (CCMC; https://ccmc.gsfc.nasa.gov) for supporting the WSA–Enlil + Cone simulation efforts presented in this work. The WSA

model was developed by C. N. Arge (currently at NASA Goddard Space Flight Center) and the Enlil model was developed by D. Odstrcil (currently at George Mason University).

DATA AVAILABILITY

Remote-sensing (EUV and WL) data from SDO, SOHO, and STEREO are openly available at the Virtual Solar Observatory (VSO; https://sdac.virtualsolar.org), while full-Sun magnetograph maps from SDO can be found at the Joint Science Operations Center (JSOC; http://jsoc.stanford.edu). These data were visualized, processed, and analysed through SUNPY (SunPy Community 2020), IDL SOLARSOFT (Freeland & Handy 1998), and the ESA JHELIOVIEWER software (Müller et al. 2017). Bepi data from the mission's cruise phase will be released to the public in the future. SolO, PSP, and STEREO-A data can be found at NASA's Coordinated Data Analysis Web (CDAWeb; https://cdaweb.gsfc.nasa.gov) data base. The OSPREI modelling suite is entirely available online and can be found at https://github.com/ckay314/OSPREI. Finally, the WSA–Enlil + Cone simulation run employed in this work can be accessed online at https://ccmc.gsfc.nasa.gov/ungrouped/SH/Helio_main.php (run id: *Erika_Palmerio_072624_SH_1*).

REFERENCES

Abraham-Shrauner B., Yun S. H., 1976, J. Geophys. Res., 81, 2097
Acuña M. H., Curtis D., Scheifele J. L., Russell C. T., Schroeder P., Szabo A., Luhmann J. G., 2008, Space Sci. Rev., 136, 203
Al-Haddad N. et al., 2013, Sol. Phys., 284, 129
Al-Haddad N., Nieves-Chinchilla T., Savani N. P., Lugaz N., Roussev I. I., 2018, Sol. Phys., 293, 73
Al-Shakarchi D. A., Morgan H., 2018, J. Geophys. Res. (Space Phys.), 123, 2535
Altschuler M. D., Newkirk G., 1969, Sol. Phys., 9, 131
Arge C. N., Luhmann J. G., Odstrcil D., Schrijver C. J., Li Y., 2004, J. Atmos. Solar-Terr. Phys., 66, 1295
Asvestari E. et al., 2021, A&A, 652, A27
Attrill G. D. R., Harra L. K., van Driel-Gesztelyi L., Démoulin P., Wülser J. P., 2007, Astron. Nachr., 328, 760
Bale S. D. et al., 2016, Space Sci. Rev., 204, 49
Balmaceda L. A., Vourlidas A., Stenborg G., Kwon R.-Y., 2022, ApJ, 931, 141
Benkhoff J. et al., 2021, Space Sci. Rev., 217, 90
Blanco J. J., Hidalgo M. A., Rodriguez-Pacheco J., Medina J., 2011, J. Atmos. Solar-Terr. Phys., 73, 1339
Bothmer V., Mrotzek N., 2017, Sol. Phys., 292, 157
Bothmer V., Schwenn R., 1998, Ann. Geophys., 16, 1
Brueckner G. E. et al., 1995, Sol. Phys., 162, 357
Burlaga L. F., 1988, J. Geophys. Res., 93, 7217
Burlaga L., Sittler E., Mariani F., Schwenn R., 1981, J. Geophys. Res., 86, 6673
Burlaga L. F., Ness N. F., Richardson J. D., Lepping R. P., 2001, Sol. Phys., 204, 399
Carcaboso F. et al., 2024, A&A, 684, A90
Case A. W. et al., 2020, ApJS, 246, 43
Colburn D. S., Sonett C. P., 1966, Space Sci. Rev., 5, 439
Davies E. E. et al., 2021, A&A, 656, A2
Davies E. E., Winslow R. M., Scolini C., Forsyth R. J., Möstl C., Lugaz N., Galvin A. B., 2022, ApJ, 933, 127
Davies E. E. et al., 2024, ApJ, 973, 51
Démoulin P., Dasso S., 2009, A&A, 498, 551
Domingo V., Fleck B., Poland A. I., 1995, Sol. Phys., 162, 1
Dumbović M. et al., 2019, ApJ, 880, 18
Farrugia C. J., Burlaga L. F., Osherovich V. A., Richardson I. G., Freeman M. P., Lepping R. P., Lazarus A. J., 1993, J. Geophys. Res., 98, 7621
Farrugia C. J. et al., 2011, J. Atmos. Solar-Terr. Phys., 73, 1254
Forbes T. G., 2000, J. Geophys. Res., 105, 23153
Fox N. J. et al., 2016, Space Sci. Rev., 204, 7
Freeland S. L., Handy B. N., 1998, Sol. Phys., 182, 497
Galvin A. B. et al., 2008, Space Sci. Rev., 136, 437
Good S. W., Kilpua E. K. J., LaMoury A. T., Forsyth R. J., Eastwood J. P., Möstl C., 2019, J. Geophys. Res. (Space Phys.), 124, 4960
Good S. W., Ala-Lahti M., Palmerio E., Kilpua E. K. J., Osmane A., 2020, ApJ, 893, 110
Green L. M., Török T., Vršnak B., Manchester W., Veronig A., 2018, Space Sci. Rev., 214, 46
Harvey J. W. et al., 1996, Science, 272, 1284
Hayashi K., Hoeksema J. T., Liu Y., Bobra M. G., Sun X. D., Norton A. A., 2015, Sol. Phys., 290, 1507
Heyner D. et al., 2021, Space Sci. Rev., 217, 52
Horbury T. S. et al., 2020, A&A, 642, A9
Howard R. A. et al., 2008, Space Sci. Rev., 136, 67
Isavnin A., Vourlidas A., Kilpua E. K. J., 2014, Sol. Phys., 289, 2141
Jin M., Manchester W. B., van der Holst B., Sokolov I., Tóth G., Vourlidas A., de Koning C. A., Gombosi T. I., 2017, ApJ, 834, 172
Kaiser M. L., Kucera T. A., Davila J. M., St. Cyr O. C., Guhathakurta M., Christian E., 2008, Space Sci. Rev., 136, 5
Karpen J. T., Kumar P., Wyper P. F., DeVore C. R., Antiochos S. K., 2024, ApJ, 966, 27
Kasper J. C. et al., 2016, Space Sci. Rev., 204, 131
Kay C., Gopalswamy N., 2017, J. Geophys. Res. (Space Phys.), 122, 11,810
Kay C., Gopalswamy N., 2018, J. Geophys. Res. (Space Phys.), 123, 7220
Kay C., Nieves-Chinchilla T., 2021, J. Geophys. Res. (Space Phys.), 126, e28966
Kay C., Palmerio E., 2024, Space Weather, 22, e2023SW003796
Kay C., Opher M., Evans R. M., 2015, ApJ, 805, 168
Kay C., Mays M. L., Collado-Vega Y. M., 2022a, Space Weather, 20, e2021SW002914
Kay C., Nieves-Chinchilla T., Hofmeister S. J., Palmerio E., 2022b, Space Weather, 20, e2022SW003165
Kay C. et al., 2024, Space Weather, 22, e2024SW003951
Kieokaew R. et al., 2024, J. Space Weather Space Clim., 14, 19
Kilpua E. K. J. et al., 2009, Sol. Phys., 254, 325
Kilpua E. K. J., Isavnin A., Vourlidas A., Koskinen H. E. J., Rodriguez L., 2013, Ann. Geophys., 31, 1251
Kilpua E. K. J., Lumme E., Andreeova K., Isavnin A., Koskinen H. E. J., 2015, J. Geophys. Res. (Space Phys.), 120, 4112
Kilpua E., Koskinen H. E. J., Pulkkinen T. I., 2017, Living Rev. Sol. Phys., 14, 5
Kilpua E. K. J., Lugaz N., Mays M. L., Temmer M., 2019, Space Weather, 17, 498
Kilpua E. K. J. et al., 2021, A&A, 656, A8
Kubicka M., Möstl C., Amerstorfer T., Boakes P. D., Feng L., Eastwood J. P., Törmänen O., 2016, ApJ, 833, 255
Laker R. et al., 2024, Space Weather, 22, e2023SW003628
Laperre B., Amaya J., Lapenta G., 2020, Front. Astron. Space Sci., 7, 39
Lavraud B., Owens M. J., Rouillard A. P., 2011, Sol. Phys., 270, 285
Ledvina V. E., Palmerio E., Kay C., Al-Haddad N., Riley P., 2023, A&A, 673, A96
Lee J., Karpen J. T., Liu C., Wang H., 2020, ApJ, 893, 158
Lemen J. R. et al., 2012, Sol. Phys., 275, 17
Lepping R. P., Jones J. A., Burlaga L. F., 1990, J. Geophys. Res., 95, 11957
Liu Y., Richardson J. D., Belcher J. W., Wang C., Hu Q., Kasper J. C., 2006, J. Geophys. Res., 111, A12S03
Liu Y. D., Hu H., Wang C., Luhmann J. G., Richardson J. D., Yang Z., Wang R., 2016, ApJS, 222, 23
Liu Y. A., Liu Y. D., Hu H., Wang R., Zhao X., 2018, ApJ, 854, 126
Longcope D. W., 2005, Living Rev. Sol. Phys., 2, 7
Lugaz N., Farrugia C. J., Davies J. A., Möstl C., Davis C. J., Roussev I. I., Temmer M., 2012, ApJ, 759, 68
Lugaz N., Temmer M., Wang Y., Farrugia C. J., 2017, Sol. Phys., 292, 64
Lugaz N., Farrugia C. J., Winslow R. M., Al-Haddad N., Galvin A. B., Nieves-Chinchilla T., Lee C. O., Janvier M., 2018, ApJ, 864, L7

Lugaz N. et al., 2022, ApJ, 929, 149
Luhmann J. G. et al., 2008, Space Sci. Rev., 136, 117
Luhmann J. G., Gopalswamy N., Jian L. K., Lugaz N., 2020, Sol. Phys., 295, 61
Lynch B. J., Masson S., Li Y., DeVore C. R., Luhmann J. G., Antiochos S. K., Fisher G. H., 2016, J. Geophys. Res. (Space Phys.), 121, 10677
Maharana A., Cramer W. D., Samara E., Scolini C., Raeder J., Poedts S., 2024, Space Weather, 22, e2023SW003715
Manchester W., Kilpua E. K. J., Liu Y. D., Lugaz N., Riley P., Török T., Vršnak B., 2017, Space Sci. Rev., 212, 1159
Maunder M. L., Foullon C., Forsyth R., Barnes D., Davies J., 2022, Sol. Phys., 297, 148
Mays M. L. et al., 2015, ApJ, 812, 145
Möstl C. et al., 2018, Space Weather, 16, 216
Möstl C. et al., 2022, ApJ, 924, L6
Müller D. et al., 2017, A&A, 606, A10
Müller D. et al., 2020, A&A, 642, A1
Mulligan T., Russell C. T., Luhmann J. G., 1998, Geophys. Res. Lett., 25, 2959
Nieves-Chinchilla T., Vourlidas A., Raymond J. C., Linton M. G., Al-haddad N., Savani N. P., Szabo A., Hidalgo M. A., 2018a, Sol. Phys., 293, 25
Nieves-Chinchilla T., Linton M. G., Hidalgo M. A., Vourlidas A., 2018b, ApJ, 861, 139
Odstrcil D., 2003, Adv. Space Res., 32, 497
Odstrcil D., 2023, Front. Astron. Space Sci., 10, 1226992
Owen C. J. et al., 2020, A&A, 642, A16
Owens M. J., 2020, Sol. Phys., 295, 148
Owens M. J., Cargill P. J., Pagel C., Siscoe G. L., Crooker N. U., 2005, J. Geophys. Res., 110, A01105
Pal S., Dash S., Nandy D., 2020, Geophys. Res. Lett., 47, e2019GL086372
Pal S., Lynch B. J., Good S. W., Palmerio E., Asvestari E., Pomoell J., Stevens M. L., Kilpua E. K. J., 2022, Front. Astron. Space Sci., 9, 903676
Palmerio E., Kilpua E. K. J., James A. W., Green L. M., Pomoell J., Isavnin A., Valori G., 2017, Sol. Phys., 292, 39
Palmerio E. et al., 2018, Space Weather, 16, 442
Palmerio E. et al., 2021a, Space Weather, 19, e2020SW002654
Palmerio E. et al., 2021b, J. Geophys. Res. (Space Phys.), 126, e2021JA029770
Palmerio E., Kay C., Al-Haddad N., Lynch B. J., Yu W., Stevens M. L., Pal S., Lee C. O., 2021c, ApJ, 920, 65
Palmerio E. et al., 2022a, Space Weather, 20, e2021SW002993
Palmerio E. et al., 2022b, Space Weather, 20, e2022SW003215
Palmerio E. et al., 2023a, BAAS, 55, 307
Palmerio E., Maharana A., Lynch B. J., Scolini C., Good S. W., Pomoell J., Isavnin A., Kilpua E. K. J., 2023b, ApJ, 958, 91
Palmerio E. et al., 2024a, J. Space Weather Space Clim., 14, 3
Palmerio E. et al., 2024b, ApJ, 963, 108
Paschmann G., Schwartz S. J., 2000, in Harris R. A., ed., ESA SP-449: Cluster-II Workshop Multiscale / Multipoint Plasma Measurements. ESA, Noordwijk, p. 99
Patsourakos S., Vourlidas A., Kliem B., 2010, A&A, 522, A100
Patsourakos S. et al., 2020, Space Sci. Rev., 216, 131
Pesnell W. D., Thompson B. J., Chamberlin P. C., 2012, Sol. Phys., 275, 3
Pulkkinen T. I., Partamies N., Huttunen K. E. J., Reeves G. D., Koskinen H. E. J., 2007, Geophys. Res. Lett., 34, L02105
Regnault F., Al-Haddad N., Lugaz N., Farrugia C. J., Yu W., Zhuang B., Davies E. E., 2024, ApJ, 962, 190
Richardson I. G., Cane H. V., 2010, Sol. Phys., 264, 189
Richardson J. D., Liu Y., Wang C., Burlaga L. F., 2006, Adv. Space Res., 38, 528
Riley P., Linker J. A., Mikić Z., Odstrcil D., Zurbuchen T. H., Lario D., Lepping R. P., 2003, J. Geophys. Res., 108, 1272
Riley P. et al., 2004, J. Atmos. Solar-Terr. Phys., 66, 1321
Riley P. et al., 2018, Space Weather, 16, 1245
Ruffenach A. et al., 2012, J. Geophys. Res., 117, A09101
Ruffenach A. et al., 2015, J. Geophys. Res. (Space Phys.), 120, 43
Salman T. M., Winslow R. M., Lugaz N., 2020, J. Geophys. Res. (Space Phys.), 125, e2019JA027084
Samara E., Laperre B., Kieokaew R., Temmer M., Verbeke C., Rodriguez L., Magdalenić J., Poedts S., 2022, ApJ, 927, 187
Sarkar R., Srivastava N., Gopalswamy N., Kilpua E., 2024, ApJS, 273, 36
Savani N. P., Owens M. J., Rouillard A. P., Forsyth R. J., Davies J. A., 2010, ApJ, 714, L128
Scherrer P. H. et al., 2012, Sol. Phys., 275, 207
Scolini C., Winslow R. M., Lugaz N., Poedts S., 2023, ApJ, 944, 46
Sterling A. C., Moore R. L., 2001, ApJ, 560, 1045
Subramanian P., Arunbabu K. P., Vourlidas A., Mauriya A., 2014, ApJ, 790, 125
SunPy Community, 2020, ApJ, 890, 68
Szabo A., Ho G., Jian L., Lario D., Nieves-Chinchilla T., 2023, BAAS, 55, 384
Temmer M., 2021, Living Rev. Sol. Phys., 18, 4
Thernisien A., 2011, ApJS, 194, 33
Thompson B. J., Plunkett S. P., Gurman J. B., Newmark J. S., St. Cyr O. C., Michels D. J., 1998, Geophys. Res. Lett., 25, 2465
Török T. et al., 2018, ApJ, 856, 75
Trotta D. et al., 2022, Front. Astron. Space Sci., 9, 1005672
Trotta D. et al., 2024a, ApJ, 962, 147
Trotta D. et al., 2024b, ApJ, 971, L35
Verbeke C. et al., 2019, Space Weather, 17, 6
Verbeke C. et al., 2023, Adv. Space Res., 72, 5243
Vourlidas A., Webb D. F., 2018, ApJ, 861, 103
Vourlidas A., Colaninno R., Nieves-Chinchilla T., Stenborg G., 2011, ApJ, 733, L23
Vršnak B. et al., 2013, Sol. Phys., 285, 295
Vršnak B. et al., 2019, ApJ, 877, 77
von Steiger R., Richardson J. D., 2006, Space Sci. Rev., 123, 111
Wang Y. M., Sheeley N. R., Jr, 1992, ApJ, 392, 310
Wang Y., Wang B., Shen C., Shen F., Lugaz N., 2014, J. Geophys. Res. (Space Phys.), 119, 5117
Webb D. F., Vourlidas A., 2016, Sol. Phys., 291, 3725
Weiss A. J. et al., 2021, A&A, 656, A13
Winslow R. M., Scolini C., Lugaz N., Galvin A. B., 2021, ApJ, 916, 40
Witasse O. et al., 2017, J. Geophys. Res. (Space Phys.), 122, 7865
Wuelser J.-P. et al., 2004, in Fineschi S., Gummin M. A., eds, Proc. SPIE Conf. Ser. Vol. 5171, Telescopes and Instrumentation for Solar Astrophysics. SPIE, Bellingham, p. 111
Wyper P. F., DeVore C. R., 2016, ApJ, 820, 77
Wyper P. F., DeVore C. R., Karpen J. T., Lynch B. J., 2016, ApJ, 827, 4
Xie H., Gopalswamy N., Akiyama S., 2021, ApJ, 922, 64
Yu W., Al-Haddad N., Farrugia C. J., Lugaz N., Regnault F., Galvin A., 2022, ApJ, 937, 86
Yurchyshyn V., Hu Q., Lepping R. P., Lynch B. J., Krall J., 2007, Adv. Space Res., 40, 1821
Zhang Q., 2024, Rev. Mod. Plasma Phys., 8, 7
Zhang J. et al., 2007, J. Geophys. Res., 112, A10102
Zhuang B., Lugaz N., Temmer M., Gou T., Al-Haddad N., 2022, ApJ, 933, 169
Zuccarello F. P., Bemporad A., Jacobs C., Mierla M., Poedts S., Zuccarello F., 2012, ApJ, 744, 66
Zurbuchen T. H., Richardson I. G., 2006, Space Sci. Rev., 123, 31

SUPPORTING INFORMATION

Supplementary data are available at *MNRAS* online.

SuppVideo1.mp4

SuppVideo2.mp4

SuppVideo3.mp4

SuppVideo4.mp4

Please note: Oxford University Press is not responsible for the content or functionality of any supporting materials supplied by the authors.

Any queries (other than missing material) should be directed to the corresponding author for the article.

APPENDIX A: CME PROPAGATION WITH WSA–ENLIL

To verify that the expected *in situ* impacts from the 2021 September 23 event are reasonable in terms of arrival times at the different locations, we model the inner heliospheric propagation of the CME using the coupled WSA–Enlil model. WSA operates in the so-called coronal domain of the simulation and employs magnetic field maps of the solar photosphere to generate the ambient conditions in the range 1–21.5 $R_\odot$. Enlil operates in the so-called heliospheric domain of the simulation and uses WSA outputs at 21.5 $R_\odot$ (or 0.1 au) to model the solar wind and interplanetary magnetic field up to a user-defined heliocentric distance – in this work, we set our outer boundary to 1.1 au. Within this framework, CMEs can be inserted at the interface between the WSA and Enlil domains, i.e. 0.1 au, corresponding to the outer corona. The employed CME ejecta morphology consists of a tilted ellipsoid (see Mays et al. 2015) and lacks an internal magnetic field – we shall refer to this set-up as Enlil+Cone. A CME ejecta described as a hydrodynamic pulse is not appropriate for modelling and reproducing its magnetic field configuration; nevertheless, the WSA–Enlil + Cone framework has been shown to be adequate for evaluating multispacecraft CME arrival times (Odstrcil 2023).

The photospheric maps that we use as input for WSA are daily-updated zero-point-corrected synoptic magnetograms from the National Solar Observatory Global Oscillation Network Group (Harvey et al. 1996). The input parameters for the cone CME are taken directly from the GCS reconstructions presented in Section 2.2 and Fig. 3, and the formulas to convert GCS dimensional parameters into semiminor and semimajor axes of the ellipsoidal CME cross-section can be found in Palmerio et al. (2023b, Appendix A). The CME is inserted through the inner boundary of Enlil on 2021 September 23 at 17:08 UT with a propagation direction $(\theta, \phi) = (-8^\circ, -37^\circ)$ in Stonyhurst coordinates, a tilt $\psi = 40^\circ$ (measured counterclockwise from the solar west direction), half-widths $(R_{\max}, R_{\min}) = (30^\circ, 20^\circ)$, and initial speed $V_0 = 390$ km s^{-1}. An overview of the simulation results is displayed in Fig. A1 and an animation is provided in Supplementary Video 4.

It is evident from the (modelled-versus-observed) time series comparisons shown in Fig. A1(c)–(f) that the 2021 September 23 CME is expected to impact all four spacecraft considered in this work, i.e. Bepi, SolO, PSP, and STEREO-A. The simulated arrival times at each location are remarkably close to the corresponding spacecraft measurements, the modelled impacts being ∼1 h late at Bepi, ∼3 h early at SolO, ∼4 h late at PSP, and ∼3 h late at STEREO-A – all comfortably within the current CME arrival time uncertainties of $\gtrsim$10 h (Kay et al. 2024). Additionally, it is possible to note in Fig. A1(a–b) and Supplementary Video 4 that the CME is expected to encounter Bepi through its very eastern flank, SolO through its nose, and PSP as well as STEREO-A at intermediate distances from the apex. Overall, the WSA–Enlil + Cone simulation showcased here demonstrates that our assessment and interpretation of the large-scale heliospheric evolution of the 2021 September 23 event is self-consistent.

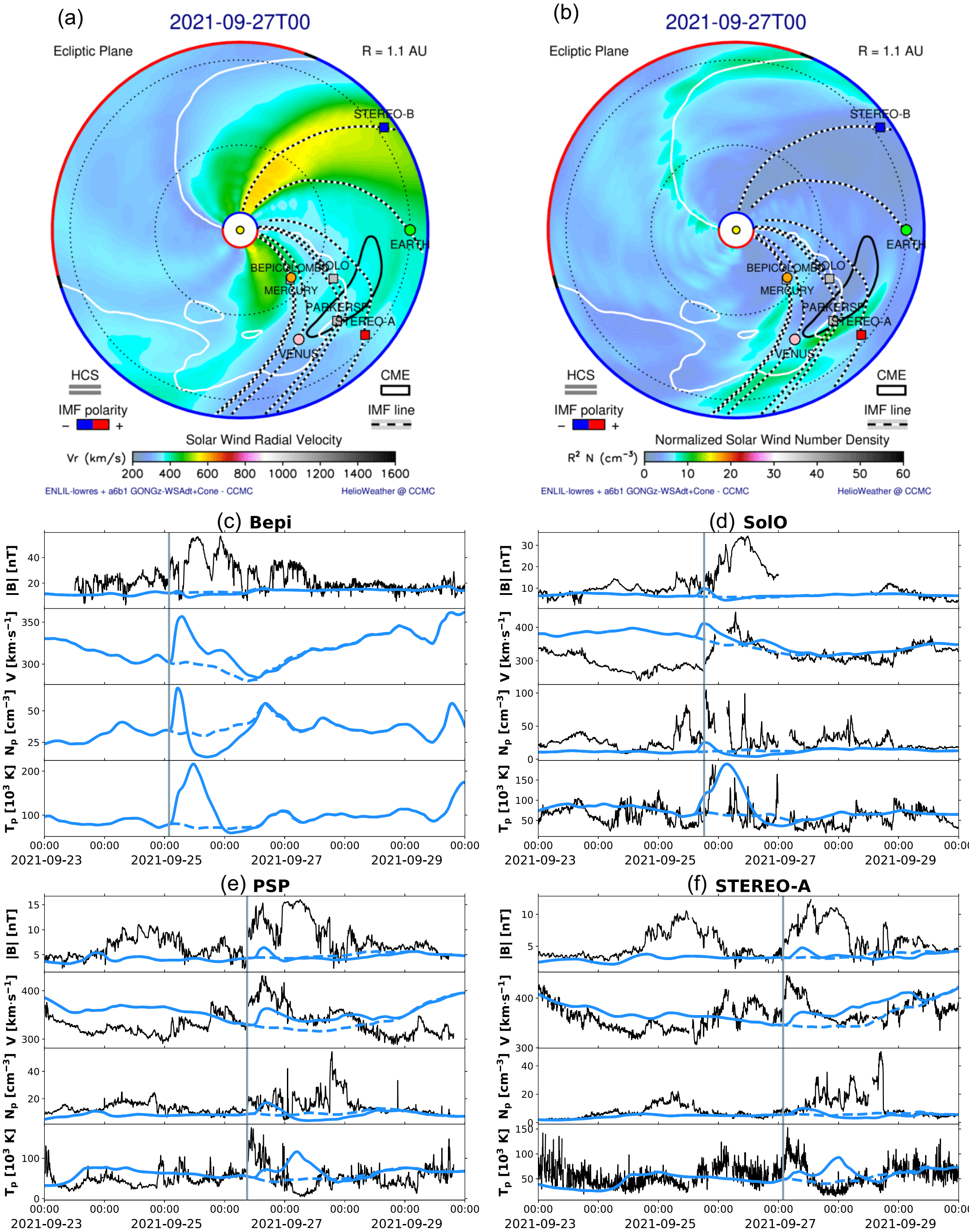

Figure A1. Overview of the WSA–Enlil+Cone simulation run and comparison of the modelled results at the four spacecraft of interest. The top row shows views on the ecliptic plane of the solar wind (a) radial speed and (b) normalized number density within the simulation's heliospheric domain (0.1–1.1 au), showing the CME (outlined with a solid contour) about to impact PSP. An animated version of panels (a) and (b) is featured in Supplementary Video 4. The remaining panels display WSA–Enlil simulation results presented against spacecraft measurements at (c) Bepi, (d) SolO, (e) PSP, and (f) STEREO-A. Observations are shown in thinner curves, while modelled time series are shown in thicker curves – where the solid line indicates the WSA–Enlil + Cone simulation run and the dashed line provides the corresponding WSA–Enlil ambient run (without the CME). The observed interplanetary shock arrival at each location is marked with a vertical solid line.

This paper has been typeset from a TEX/LATEX file prepared by the author.